JOURNAL OF GEOPHYSICAL RESEARCH, VOL. 98, NO. B3, PAGES 4355–4375, MARCH 10, 1993

The Three-Dimensional Structure of Kilauea Volcano, Hawaii, From Travel Time Tomography

LINDA R. ROWAN AND ROBERT W. CLAYTON

Seismological Laboratory, California Institute of Technology, Pasadena

A linear, travel time tomography study of the most active shield volcano of the world, Kilauea Volcano, Hawaii, was undertaken to determine the lateral heterogeneities produced by its intricate magmatic and tectonic environment. Kilauea provides an ideal setting to do tomography because of its dense seismograph array and many local earthquakes that allow excellent ray coverage of complex subsurface features. Local *P* wave data from ~12,295 events were inverted using a one-dimensional layered velocity model. Inversions were done for two cell sizes (5 × 5 × 5 km and 1 × 1 × 1 km) to resolve structural regions on different length scales. This study provided a view of the average velocity variations relative to a one-dimensional velocity model. Analysis and interpretation of the tomographic images allowed us to infer the following model. The main shallow magma reservoir is delineated by a slow velocity region southeast of the summit from 0 to 2 km depth. There is a distinct high velocity region centered northwest of the summit from 0 to 2 km depth that represents a cap of dense, intrusive dikes surrounding the magma chamber. We suggest that the shallow reservoir is a narrow, compartmentalized region of sills and dikes, centered just south-southeast of Halemaumau caldera. Below the main reservoir, the summit is imaged as a slightly fast region from 5 to 10 km in the coarse model indicating that the main conduit is structurally defined by an intrusive dike complex until about 10 km. The rift zones of Kilauea are imaged as major, high velocity entities, widening to the south with depth until 6 km. These fast anomalies are related to the sheeted dike complexes along the rifts. On a finer scale, slow anomalies suggest the presence of magma pockets centered at 0–2 km depth beneath Mauna Ulu, Makaopuhi and Puu Oo, along the east rift zone (ERZ). Two significant high velocity regions along the lower ERZ near Kalalua and Kaliu are inferred to represent intrusive barriers to magma injection along the shallow (0–4 km) ERZ conduit. The southwest rift zone may have an intrusive barrier related to a high velocity region just southwest of Mauna Iki. The Hilina and Kaoiki fault zones are imaged as slow features at shallow depths (< 5 km) related to the open fractures and scarps along the normal faults. The Koae fault system is imaged as a slightly fast shallow structure (< 6 km) possibly related to intrusive diking from the adjacent rift zones that fill and may even induce the extensional structures associated with this complex fault zone. Continued inversions with the immense amount of seismic data collected for Hawaiian events will allow the detailed development of a three-dimensional structural model for Kilauea. Such a model will be extremely useful to seismologists and petrologists alike for understanding the tectonic growth and magmatic evolution of this dynamic shield volcano.

INTRODUCTION

Kilauea is the youngest, most historically active shield volcano of the Hawaiian - Emperor Volcanic Chain. Located on the southeastern coast of the Island of Hawaii (Figure 1), its subtle relief represents the southernmost subaerial volcano created by the hotspot swell beneath the island. Kilauea's isolation from continental crustal structure and contamination, as an intraplate, oceanic volcano, and its relation to hotspot theory make it one of the most intensely studied volcanoes of the world. Its accessibility, relative simplicity compared to interplate boundaries and the large amount of data obtained through years of study, make Kilauea the most logical and feasible volcano to attempt to model in three dimensions. Our goal is to provide a detailed image of the lateral and vertical velocity heterogeneities of Kilauea that can be used to infer its magmatic structure. Such insight may improve our understanding of other processes such as hotspot dynamics, magma genesis and propagation, magma chamber structure, fault structure mechanisms and dike formation and propagation.

Paper number 92JB02531.
0148-0227/93/92JB-02531$05.00

Surface Structure

Kilauea is a broad, subtle shield volcano rising to a summit elevation of about 1.24 km and covering about 1500 km^2 (Figure 1). There are six prominent structural provinces, the summit caldera, two rift zones and three fault systems (Figure 2) that have been defined and studied by various workers [e.g., *Swanson et al.*, 1976]. We have organized and concentrated our study on extending the structural interpretation of these surface features into the shallow subsurface (~20 km).

The southwest rift zone (SWRZ) and east rift zone (ERZ) extend from the summit as subtle constructional ridges. They are delineated along their crests by cones, craters and fissures and are the source of almost all non-summit eruptions. The rift zones separate Kilauea into a stable north flank, buttressed by Mauna Loa, and a mobile south flank, which extends into the ocean. The subaerial ERZ is 60 km long, 4–6 km wide and has been divided into three segments. The upper segment (from Halemaumau Caldera to Makaopuhi Crater) is separated from the middle segment (from Makaopuhi to Heiheiahulu) and the lower segment (from Heiheiahulu to the coast) by a significant bend in the rift that has been attributed to the southward migration of the south flank [*Kinoshita et al.*, 1963; *Swanson et al.*, 1976]. The SWRZ extends approximately 30 km southwest

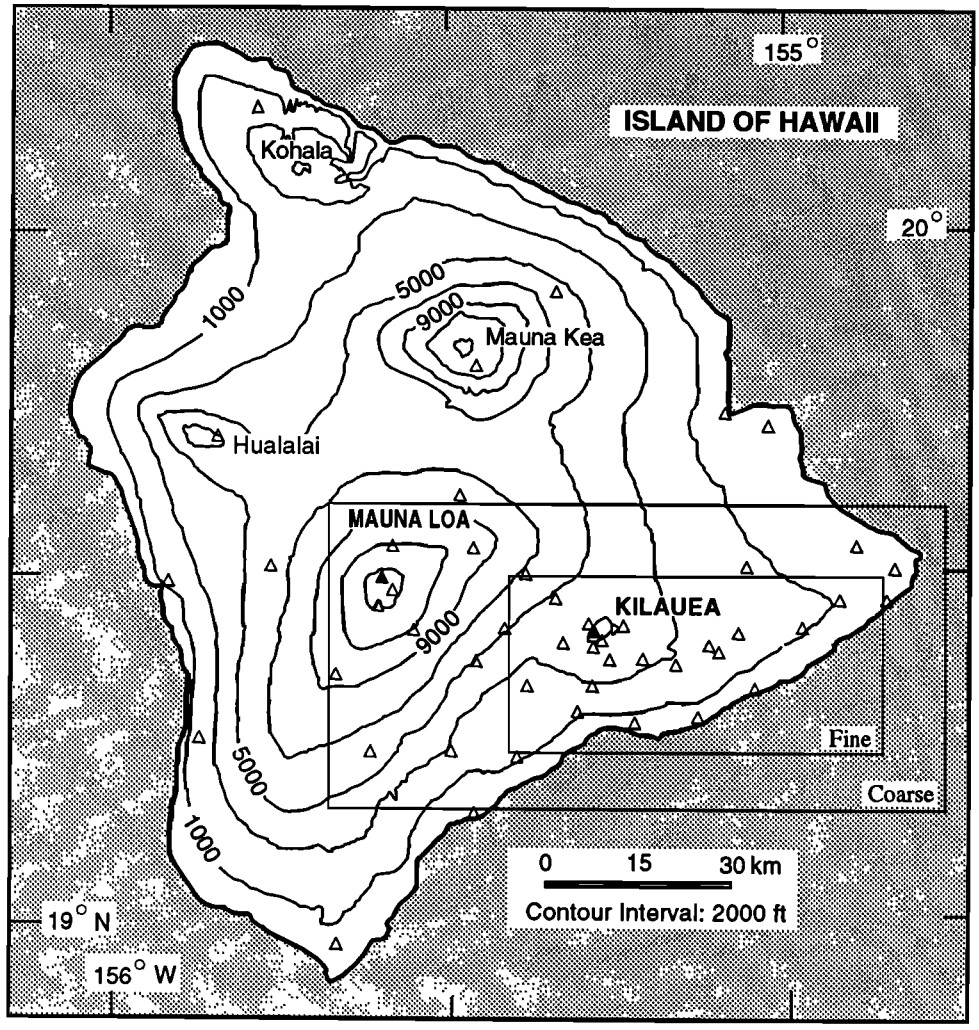

Fig. 1. Topographic map of the Island of Hawaii showing the five volcanoes and the seismographic array. Each station is labeled by a triangle except for two stations that are on other islands. The two solid triangles are stations on which we centered the caldera symbols in our model images. The large and small rectangles show the areal extent of the coarse and fine model, respectively, used for the inversion.

from the summit and is a maximum of about 4 km wide on the surface. Unlike the ERZ, it does not form a well-defined constructional ridge and has fewer intrusions and eruptions than the ERZ [*Duffield et al.*, 1982]. The lack of volcanic activity and morphological development of the SWRZ is due to its more direct and significant buttressing by Mauna Loa [*Duffield et al.*, 1982; *Fornari*, 1987; *Casadevall and Dzurisin*, 1987; *Thurber and Gripp*, 1988].

The Koae fault system, a 12 km long and 3 km wide zone of scarps and fractures south of the summit, obliquely intersects both rift zones. Together with the rift zones it separates the mobile south flank from the summit of Kilauea. Most of the Koae consists of east-northeast striking normal faults that form asymmetric grabens with steep, north-facing scarps. Several workers have described the Koae as a passive tear away zone that is being moved southward as a hinge between the two rift zones by intrusion of magma into the rifts [*Duffield*, 1975; *Swanson et al.*, 1976].

The Hilina and Kaoiki are two other important fault zones, that affect the growth of the shield volcano. The Hilina fault system, located along the southern coast of the island, is a series of normal faults with south-facing scarps. These structures are controlled by gravity and sliding of the south flank seaward [*Swanson et al.*, 1976; *Crosson and Endo*, 1982; *Dvorak et al.*, 1986; *Eissler and Kanamori*, 1987; *Thurber and Gripp*, 1988]. The Kaoiki fault system parallels the SWRZ and consists of normal faults with south-facing scarps. This fault zone is part of Mauna Loa Volcano and may have served the same structural function for Mauna Loa that the Hilina system now serves for Kilauea [*Koyanagi et al.*, 1966]. We include the Kaoiki in our discussion of Kilauea because of its proximity to Kilauea and because it is currently the most seismically active fault zone on Hawaii.

Previous Studies

Early models of the summit magma reservoir are based mainly on geodetic data [*Eaton*, 1962; *Dieterich and Decker*, 1975; *Swanson et al.*, 1976; *Duffield et al.*, 1982; *Dvorak et al.*, 1983]. Several of these studies noted that the transient features of ground deformations makes it hard to determine the exact depth of the reservoir. These complex ground motions indicate a complex magma chamber consisting of sills and dikes over a 3 km wide area [*Fiske and Kinoshita* 1969; *Duffield et al.* 1982]. *Yang et al.* [1992] eliminated the

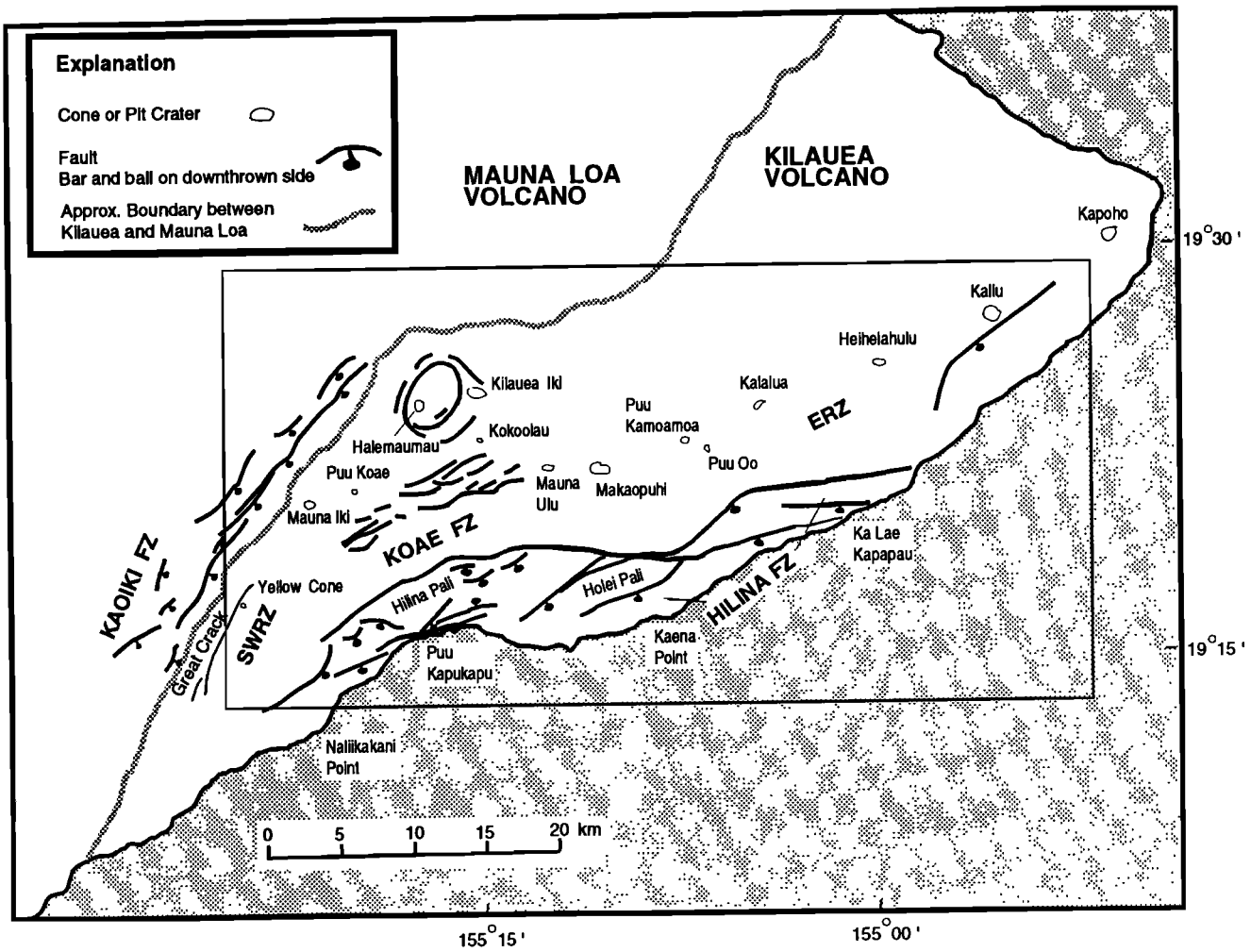

Fig. 2. Map of Kilauea Volcano and the adjacent part of Mauna Loa Volcano covered by the coarse model. Important structural regions (i.e., fault traces, cones and craters). discussed in this paper are marked. The areal extent of the fine model is shown by the smaller rectangle. Map modified from *Swanson et al.* [1976].

transient features found during many inflationary periods at Kilauea's summit from 1970–1985 by introducing dike intrusion as a secondary mechanism for ground motions. If the dike intrusion-related deformations are excluded from the geodetic data, a single magma reservoir at ~2.6 km depth, centered 2 km southeast of Halemaumau is obtained.

The complexity of the magma reservoir, as indicated by the geodetic studies, is one of the main reasons no one has imaged a large, obvious reservoir beneath the summit in previous three-dimensional seismic models [*Ellsworth and Koyanagi*, 1977; *Crosson and Koyanagi*, 1979; *Ryan et al.*, 1981; *Klein et al.*, 1987]. *Ellsworth and Koyanagi* [1977] and *Crosson and Koyanagi* [1979] inverted teleseismic and local *P* waves, respectively, and imaged high velocity features beneath the summit related to intrusive structures. *Ryan et al.* [1981] used accurately determined hypocenters to infer the intrusive outline of the magma chamber, notably a roof at 1.1–1.9 km depth, a floor at 5.7–6.5 km depth and an aseismic zone at 2–6 km depth inferred to be the shallow reservoir. More recent three-dimensional inversions have imaged some small, low velocity zones at different depths beneath Halemaumau [*Thurber*, 1984, 1987; P. Ho-Liu et al., preprint, 1991]. Thus the main shallow magma reservoir is inferred from models of ground deformation, an aseismic gap, patterns of high velocity intrusives that form the skeletal framework of the reservoir and some small, low velocity features. These observations or models do not necessarily require a large, homogeneous magma chamber.

Previous velocity models have been more successful at delineating Kilauea's rift zones than finding a shallow magma reservoir. The rifts zones stand out as dominant high velocity features in many models [*Ellsworth and Koyanagi*, 1977; *Crosson and Koyanagi*, 1979; *Thurber*, 1984 and 1987; *Hill and Zucca*, 1987]. Hill and Zucca's cross sections (Figures 37.9 and 37.10), which summarize their refraction studies and *Kinoshita et al.'s* [1963] gravity survey, suggest triangular-shaped, tholeiitic, sheeted dike complexes that extend to a depth of at least 6 km. The widening with depth of the dense intrusives agrees with *Swanson et al.'s* [1976] model of volcanic growth by the forceful intrusion of magma along the rift zones. *Klein et al.* [1987] and P. Ho-Liu et al. (preprint, 1991) have added to this model several distinct magma pockets along the rifts, including a small reservoir beneath the currently active Puu Oo eruption center. The magma is inferred to enter the ERZ through a complex pipe-shaped conduit that taps the lower part of the shallow summit magma reservoir [*Ryan et al.*, 1981; *Klein et al.*, 1987].

Our Approach

P wave travel times from local events on Kilauea and Mauna Loa recorded in 1986 were used to conduct a large-scale, linear tomographic inversion. For one set of inversions we used data from the Hawaiian Volcano Observatory (HVO) and for the second set of inversions we relocated these events using HYPOINVERSE [*Klein*, 1989]. Images produced using both data sets are presented to delineate robust anomalies that are not significantly effected by hypocenter mislocations or differences in parameters (i.e., station delays and weighting schemes) used by the location procedures. It is inappropriate to use our three-dimensional images to derive a three-dimensional velocity model, use this new model to relocate hypocenters and reinvert for new three-dimensional images because these images are ultimately dependent on the one-dimensional velocity model. A three-dimensional tomographic inversion would be more accurate and the resulting images more meaningful if an independently derived three-dimensional velocity model was used. Even with the important improvements in three-dimensional ray tracing, hypocenters are not fixed and ray paths are only approximate, making it difficult to describe the precise ray path taken around sharp velocity contrasts inferred to exist at Kilauea. A more accurate three-dimensional velocity model may be obtained by doing a detailed refraction survey where source locations and ray paths are known.

Other problems common to tomographic inversions include appropriateness of the model space, influence of ray bending and nonuniform distribution of stations and/or sources. Our approach is to describe the data, the method and define and discuss the noise introduced into our images via errors in the data and/or method. Finally, we present the average three-dimensional velocity variations of Kilauea relative to the one-dimensional velocity model and our preferred structural interpretations of these anomalies.

DATA DESCRIPTION

Hawaii is ideal for travel time tomography using local events because it has a dense seismograph array and abundant local seismicity, particularly around Kilauea. The array consists of 54 stations, of which, 42 were used for our inversions (Figure 1). Station coverage is more than adequate around Kilauea, although the network is somewhat unevenly spatially distributed with a higher density of stations on the summit and rift zones. *P* wave phase data from HVO for 12,295 local events in 1986 were used for the inversions. Most of the earthquakes were shallow (<15 km), small magnitude (<2.5) events directly related to magma movement and eruption episodes during the year. Figure 3*a* shows the distribution of hypocenters for the HVO data for one month. The general pattern of seismicity is representative of the pattern for the entire year's worth of data, so

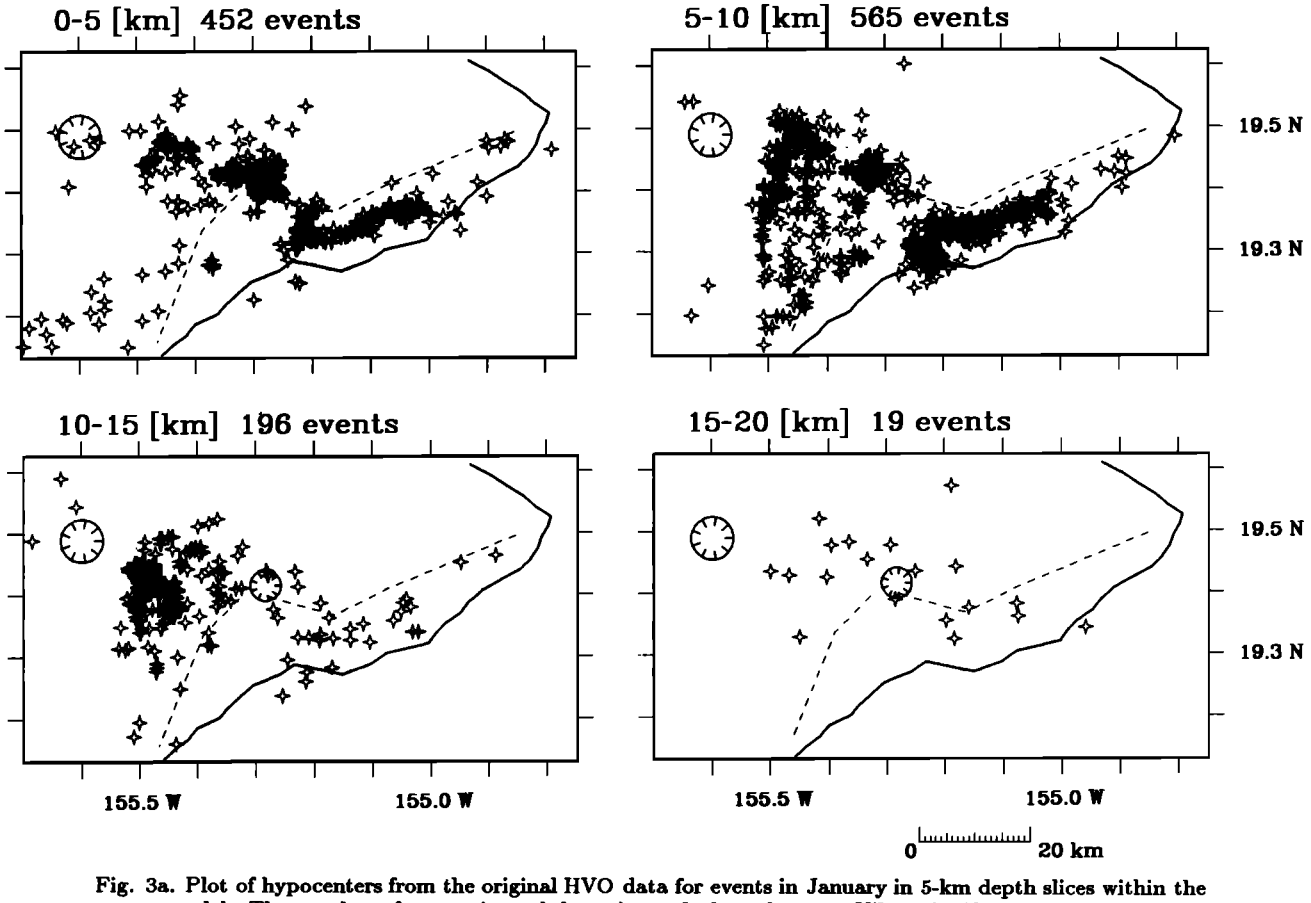

Fig. 3a. Plot of hypocenters from the original HVO data for events in January in 5-km depth slices within the coarse model. The number of events in each layer is marked on the top. Kilauea's rift zones are marked by the dashed lines. The southeastern coastline of Hawaii is marked by the solid line. Kilauea caldera, centered on station NPT, the north pit of Halemaumau, (Figure 1) is shown by the small caldera symbol. Mauna Loa caldera, centered on station MOK, Mokuaweoweo caldera (Figure 1), is shown by the larger caldera symbol.

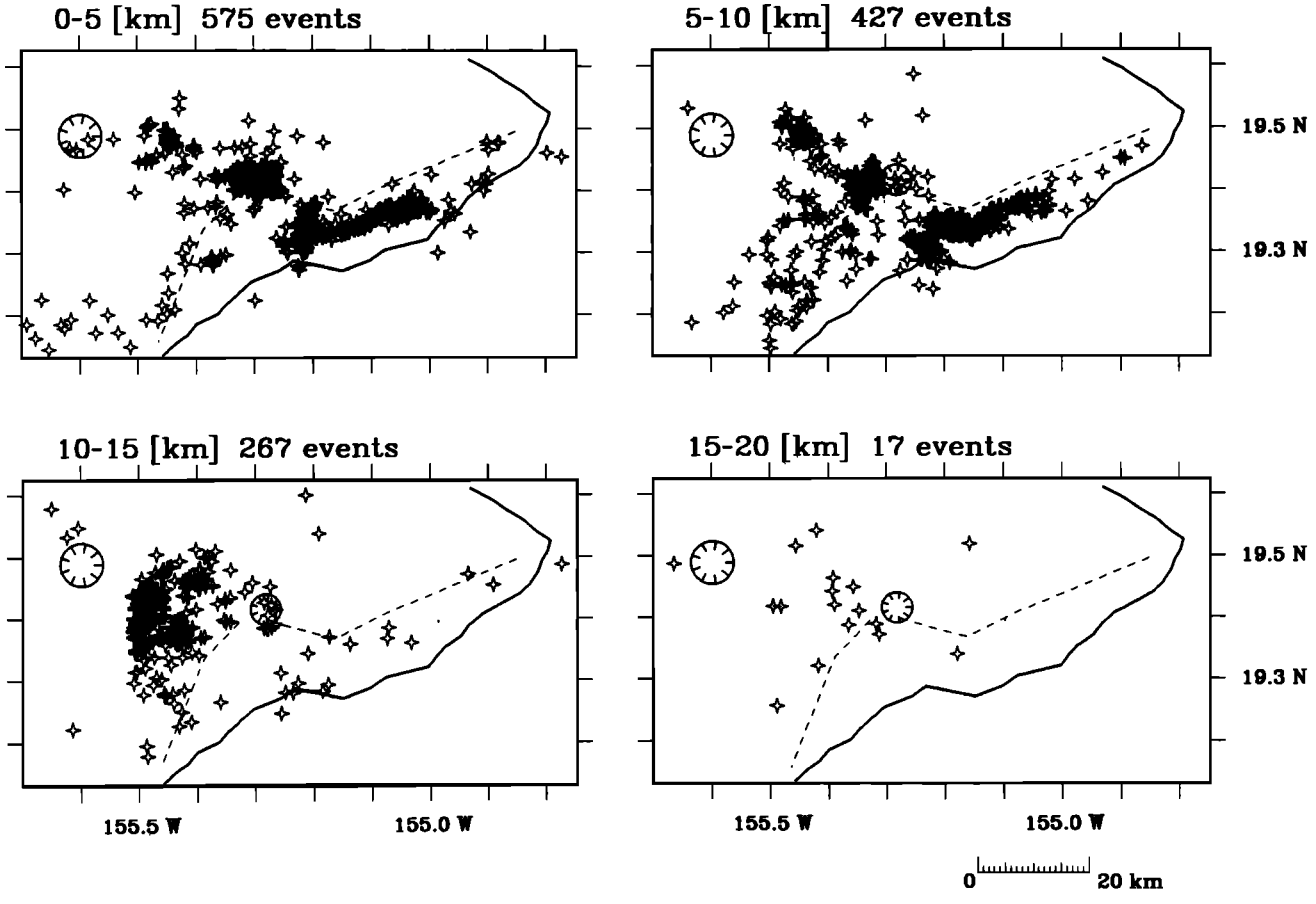

Fig. 3b. Plot of relocated hypocenters (determined using the standard layered velocity model, Figure 4, and the relocation program HYPOINVERSE [*Klein*, 1989]) for events in January in 5-km depth slices within the coarse model.

only these hypocenters are shown for clarity. The relocated hypocenters (Figure 3*b*) showed the same patterns, although the clusters are tighter and the distribution of events with depth are different from the HVO locations (see discussion in resolution and errors section).

Shallow events (<15 km) are concentrated along the Kaoiki fault system, Kilauea summit, the upper ERZ and the south flank of Kilauea. The concentration between Mauna Loa and Kilauea forms a very dense, north-south trending, linear zone from 5 to 15 km depth called the Kaoiki earthquake zone because this elongate cluster of hypocenters trends along the right-lateral strike-slip fault plane solution of the November 16, 1983, 6.6 magnitude Kaoiki earthquake (i.e., the aftershock zone). Thus these earthquakes are more tectonic in nature, representing the continued stress the dominant Mauna Loan edifice places on the smaller, very active Kilauea Volcano. Kilauea's summit shows significant activity, in two clusters, on Halemaumau caldera from 0 to 5 km depth. The eastern cluster has been attributed to the center of summit deformation and does not extend below 5 km. Events on the south flank are concentrated from 0 to 10 km depth between the summit and Kalalua Cone, which marks the eastern boundary of eruptive activity for Puu Oo. These earthquakes may be correlated directly to stresses induced by magma intrusion and propagation along the ERZ's current eruption site. It has also been suggested that the slightly more dense cluster of earthquakes along the western end of the south flank concentration, extending from just west of the bend in the ERZ southward to Puu Kapukapu, is more highly stressed. This linear zone may represent a line of breakage between different mobile blocks of the south flank [*Ryan*, 1988].

METHOD

Travel time tomography involves inverting a data set of travel time residuals (Δt) into a change of slowness (Δs) field, where slowness is the inverse of velocity. The initial travel time residual (Δt^o) is

$$\Delta t^o = TT^{obs} - TT^{raytr} \quad (1)$$

where TT^{raytr} is the calculated travel time determined by ray tracing. The velocity model used for the ray tracing is a one-dimensional, layered model modified from *Klein* [1981] (Figure 4) and is the same velocity model used by the HVO to locate earthquakes in 1986. TT^{obs} is the observed travel time computed from the data. For the HVO data, TT^{obs} is the observed arrival time of the *P* wave minus the observed origin time of the event. This model uses the HVO data as if the hypocenters were fixed and does not correct for errors in location or origin time. For the relocated hypocenters, TT^{obs} is the observed arrival time of the *P* wave minus the calculated origin time of the event. The origin time of the earthquake is adjusted during the relocation to provide the best fit to the picks [see *Klein*, 1989].

Discretization is accomplished by defining a model space

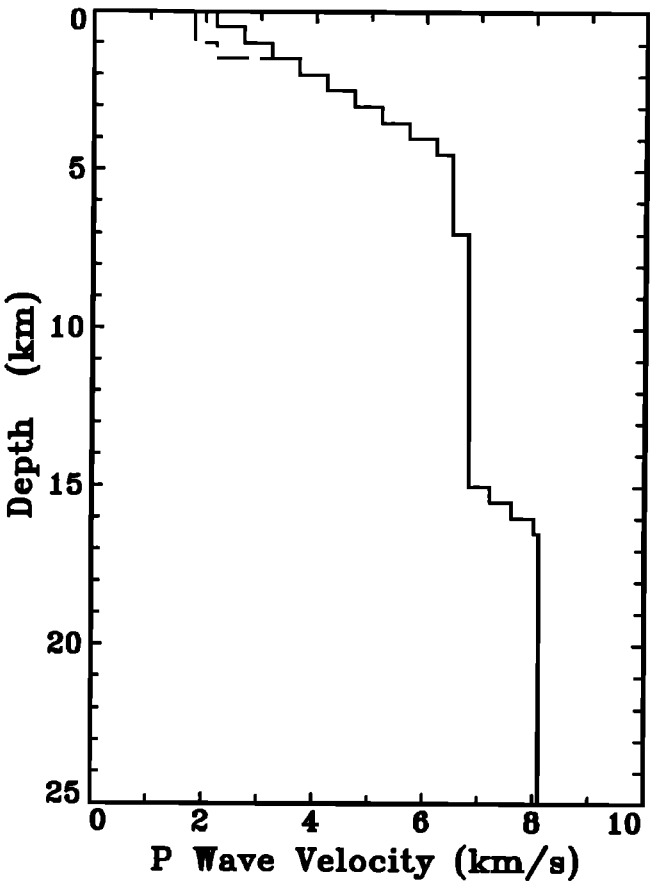

Fig. 4. One-dimensional velocity model used for the inversion. The solid line shows the standard layered velocity model modified from *Klein et al.* [1981]. It was routinely used by the HVO to locate earthquakes in 1986. The dashed line shows the modified layered velocity model used to determine the appropriateness of lower velocity layers. The shallow part of this velocity model is modified from *Hill* [1969] and *Crosson and Koyanagi* [1979], who suggested a P wave velocity of as low as 1.8 km/s for the shallowest velocity layer. Below 1.5 km the model is the same as the original model.

of three-dimensional cells over a change of slowness field. Two models with different cell sizes (Figures 1 and 2) were chosen for the tomographic inversions. The coarse model is 100 km (E-W) by 55 km (N-S) by 50 km (depth) with cell sizes of 5 × 5 × 5 km and it covers Kilauea and the southeastern part of Mauna Loa, including its summit. The fine model is 60 × 30 × 50 km with cell sizes of 1 × 1 × 1 km and it covers Kilauea's summit, rift zones, south flank and part of the Kaoiki fault system. Given the relatively gentle topography of Kilauea, no correction is made for elevation and therefore the model spaces start at sea level (i.e., 0 km = sea level) and all depths are relative to sea level. Each cell contains a constant Δs and the travel time residual of the *ith* ray is:

$$\Delta t_i = \sum_j l_{ij} \Delta s_j \qquad (2)$$

where l_{ij} is the length of the *ith* ray in the *jth* cell and Δs_j is the slowness residual in the *jth* cell. To solve for the change of slowness in each cell, an iterative back projection technique is used [*Clayton and Comer*, 1983; *Hager and Clayton*, 1991]. This method can handle large Δs models with small cell sizes, providing better resolution and/or large data sets, providing more complete coverage. The basic algorithm for each iteration, k, is:

$$\Delta t_i^k = \Delta t_i^o - \sum_j l_{ij} \Delta s_j^k \qquad (3)$$

$$\Delta s_j^{up} = \frac{\sum_i (w_i^t \Delta t_i^k / L_i) l_{ij}}{\sum_i w_i^t l_{ij} + \mu} \qquad (4)$$

$$\Delta s_j^{k+1} = \Delta s_j^k + \Delta s_j^{up} \qquad (5)$$

The travel time residual, Δt_i^k, of the *ith* ray after the *kth* iteration, is the amount of time unaccounted for by the previous iteration. The initial residual, Δt_i^o, is defined by (1), while w_i^t is the weight given to the travel time residual. The updated change of slowness, Δs_j^{up} in the *jth* cell, is determined by distributing the *kth* travel time residual into each cell the ray passes through. This is done by dividing Δt by its total path length L_i and multiplying each fractional time by the length of the *ith* ray in the *jth* cell, l_{ij} (4). The numerator is then normalized by the sum of the ray lengths in each cell plus a damping factor, μ. The last equation (5) updates the change in slowness for the next iteration. The process is repeated until the standard deviation in Δs_j^{up} has converged to the point where it is changing insignificantly between iterations. For the two models presented, 50 iterations is sufficient to reduce the change in standard deviation in Δs_j^{up} between iterations by <2%.

The damping factor, μ, in the second iterative step (4) restricts the excitation of unconstrained regions of the model. It is the only adjustable input parameter and it is determined in two ways. As a first approximation, the inversion is done at a range of μ values and the resulting images are compared. Damping factors that produce images with almost no amplitude of Δs are rejected as too large (e.g., μ=100), while μ's that produce images with too many high amplitude Δs's are rejected as too small (e.g., μ=25). Secondly, the variance in Δs for a half space velocity model, for a range of μ's, is calculated using a random number set, with gaussian distribution and variance of unity, for the initial Δt's. As μ increases, the variance in Δs decreases until μ=50. Above μ=50 there is no significant reduction in the variance of Δs. Therefore μ=50 is chosen because it gives an average amplitude signal of Δs in the images and is the smallest damping factor limiting the variance of Δs for a random noise data set. The data are also filtered to limit the effect of Δt's greater than 1.0 s by clamping these "noisier" residuals to ± 1.0 s.

The resulting images are contoured to highlight velocity anomalies. The Δs images for the fine model are smoothed in two steps, because of the small size of the cells. First, the Δs values are averaged in depth by combining the anomalies of two levels to give cell sizes of 1 × 1 × 2 km. Second, the Δs values are averaged in three dimensions by taking the average of the Δs for each cell with 25% of the Δs from its adjacent cells.

RESOLUTION AND ESTIMATED ERRORS

It is important to consider the errors introduced into the inversion by noisy data, approximate ray tracing techniques and/or inadequate velocity models and to estimate the resolving power of the given models and model sizes. By do-

ing a linear inversion we have inherently introduced noise into the resulting images so interpreting any anomaly must be done with care. Several variations of the inversion, including relocating the hypocenters, using different weighting schemes in the inversion, using a different one-dimensional velocity model, using different cell sizes and shifting the coarse and fine models, were done to estimate how much noise there is in the different images and to delineate robust anomalies. The idea is to eliminate poorly resolved areas using the model resolution tests and reject noisy or unstable anomalies in well-resolved areas by comparing the different strengths and weaknesses of the different inversions. We have not shown the results of all the different inversions because many of these images are similar to one another. We have presented the residual slowness images that show the most variation and in the following discussion we have tried to explain why these differences occur.

Model Resolution

It is impractical to calculate the entire resolution matrix for each model because of its immense size. An estimate of the resolution in each cell can be made using impulse tests, although how the resolution correlates between cells cannot be specifically addressed by these tests. In order to interpret the results of these tests, ray coverage in the model spaces must be determined. Good ray coverage is necessary to provide adequate resolution and to limit the effect of errors in the data.

A large number of rays crossing the cell at a wide range of azimuths indicates good ray coverage. The ray coverage is depicted in Figures 5 and 6 for the two models, using the two data sets (HVO and relocated hypocenters) where each plot shows the density of rays traveling through each cell. Coverage is excellent for both models, using either data set, with >75% of the cells being hit by rays to a depth of at least 20 km. The poorest spatial density occurs along the north flank of Kilauea and some regions along the lower ERZ, particularly with increasing depth. Thus lateral velocity variations in these border regions are suspect and should not be interpreted as structures.

Impulse testing involves putting a synthetic change of slowness anomaly in certain cells, setting the other cells to zero Δs, forward modeling and inverting the data. If the resolution is good, the synthetic anomalies input should be reproduced with the same intensity and shape. The shape of the anomaly is contoured so well-resolved features produce

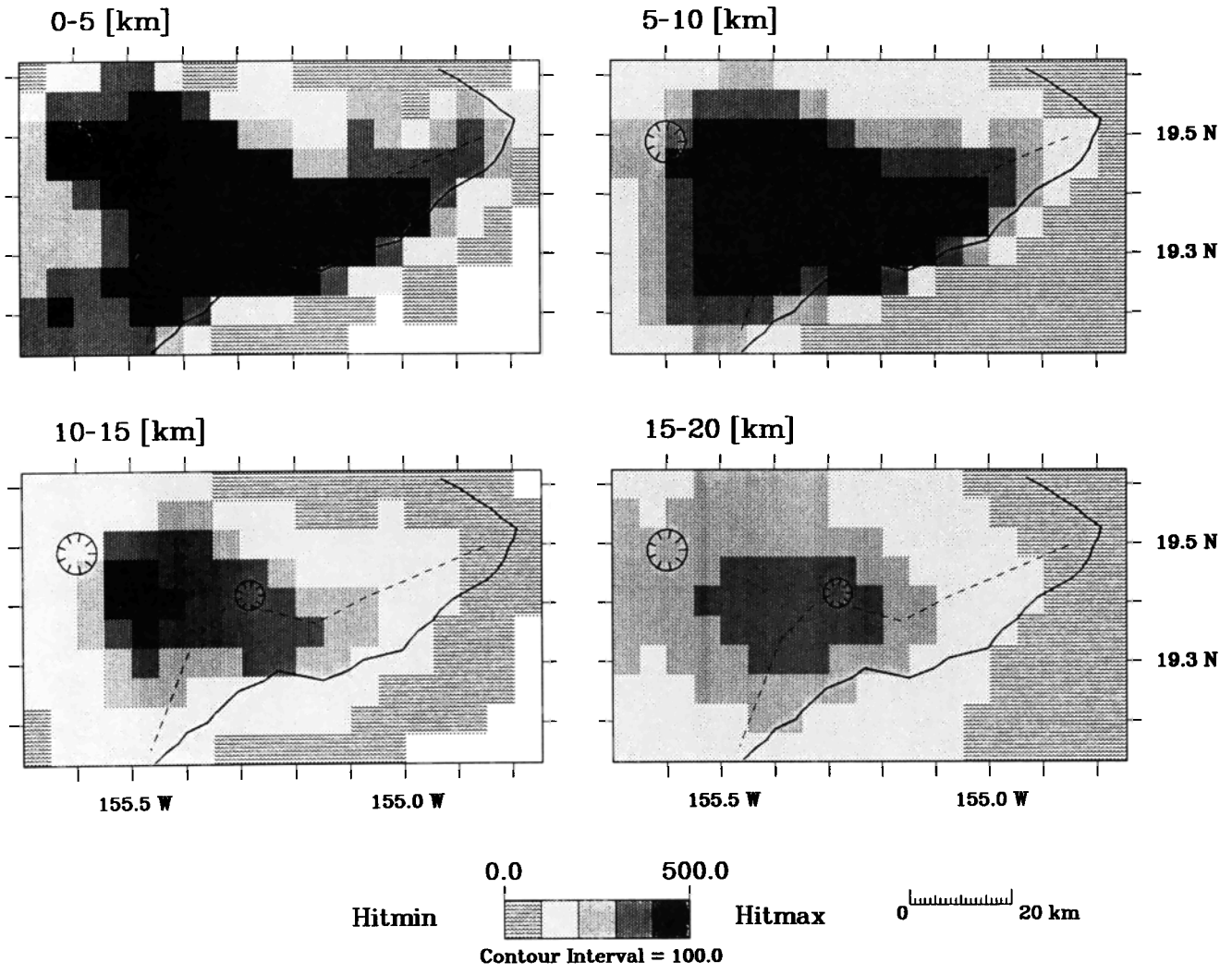

Fig. 5a. Hit count plots showing the ray coverage of the HVO hypocenters for the coarse model shown in 5-km depth slices. The hit count is the number of rays passing through each cell of the three-dimensional model.

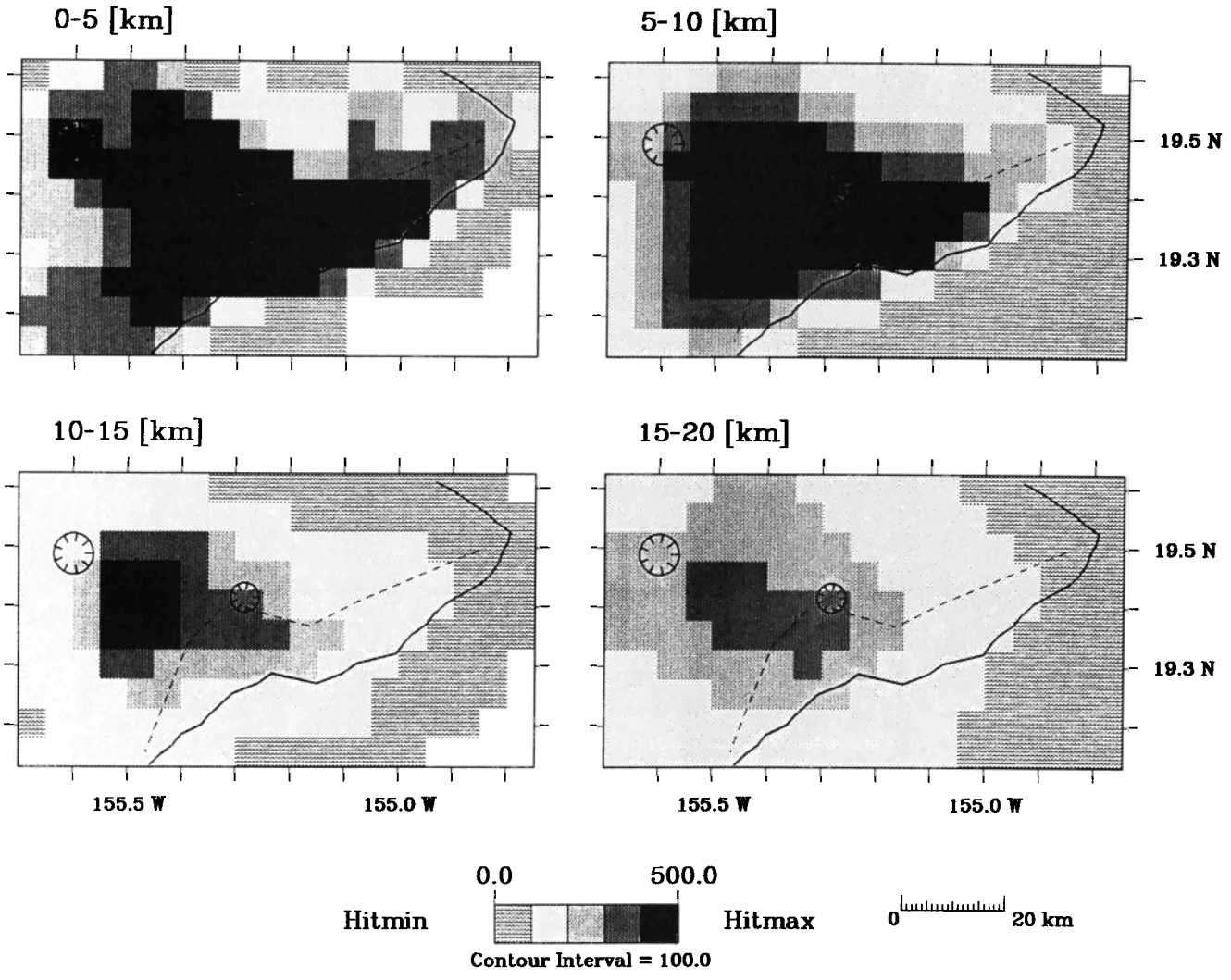

Fig. 5b. Hit count plots showing the ray coverage for the relocated hypocenters (determined using the standard layered velocity model and HYPOINVERSE [*Klein*, 1989].)

a bull's eye-shaped pattern with the maximum amplitude in the center and the smallest amplitude defining the edge of the cell. Poor resolution is indicated by a loss of amplitude or smearing of the synthetic anomalies. Smearing is due to biased azimuthal coverage, where most of the rays are traveling in one general direction and/or poor ray coverage.

The value of each synthetic anomaly is just larger than the maximum Δs obtained in the actual inversion, so these tests approach a realistic limit of the maximum signal or noise in the data. Synthetic anomaly locations are chosen to provide coverage of the important, inferred structures (i.e., the summit magma reservoir) and questionable anomalies (i.e., the north flank of Kilauea). Choosing specific locations may bias the tests, but enough different locations were tested to insure adequate and even coverage of the models. Since the ray coverage is similar for the HVO hypocenters and the relocated hypocenters, only the impulse test results using the relocated hypocenters are shown.

Synthetic anomalies are relatively well resolved in the coarse model (Figure 7). A slowness residual, Δs, of 0.05 s km^{-1}, was inserted into each depth slice separately. The results indicate that many large amplitude anomalies add noise to the slowness images. The noise produces small, slightly fast features along the edges of the covered areas. For the real inversions, there are few large amplitude anomalies, so this added noise is insignificant. To check this hypothesis, only 4 synthetic Δs's were introduced in the shallowest layer and no added noise (i.e., fast regions in other cells) was produced in the images. Overall, the resolvability is excellent around Kilauea until about 30–35 km depth where the intensity of the anomalies is significantly reduced. Slownesses on the northern boundary of the coarse model are smeared and poorly resolved. Anomalies along the lower ERZ and near Mauna Loa also indicate poorer resolution at about 15–20 km and resolution decreases with depth. Beginning at 15 km depth, there is also a slight east-west smearing of some features.

Impulse tests applied to the fine model (Figure 8) with a Δs of 0.1 s km^{-1} produced poorer resolution than the coarse model. From 0 to 1 km the resolution is good around the summit but rather poor near the bend in the ERZ and near Yellow Cone on the SWRZ. Only 20–30% of the synthetics in these areas are reproduced and there is lateral smearing of some anomalies, with small fast zones added to the images. The best resolution is obtained at Kilauea summit, with >85% of the anomaly reproduced in the first 3 km,

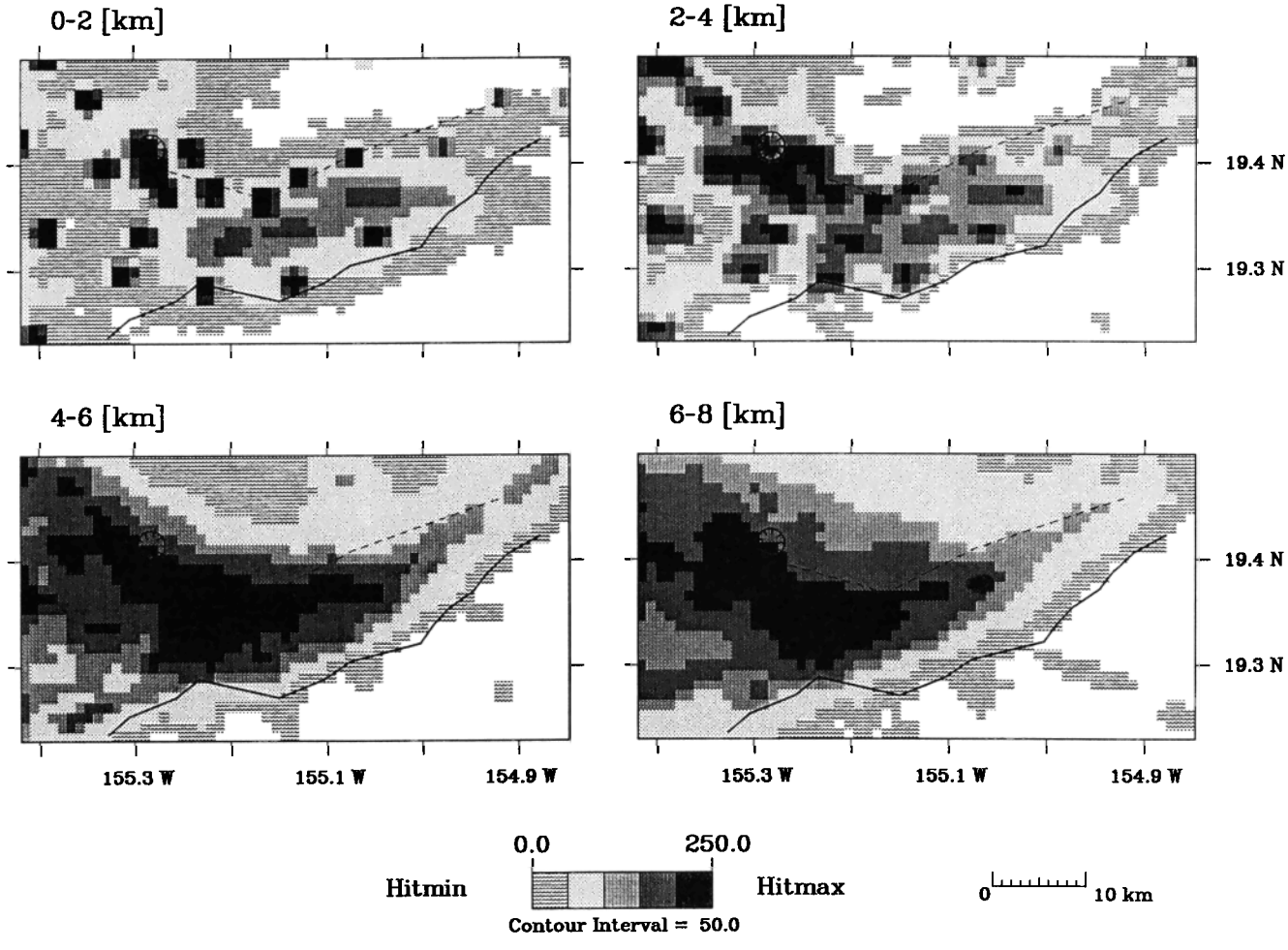

Fig. 6a. Hit count plots showing the ray coverage of the HVO hypocenters for the fine model shown in 2-km depth slices.

>60% recovered to 6 km and >30% recovered to 8 km. Below 2 km, the three synthetics near the bend in the ERZ and the synthetic near Yellow Cone on the SWRZ are fairly well resolved (most > 50%) with a small amount of east-west smearing of the anomalies. For the other synthetics less than half of the Δs is recovered and on average only 20–30% is reproduced, with some smearing of the anomaly. There is also some minor (less than 10% of the initial synthetic) smearing into different depth levels, which is not seen in the coarse model impulse tests. Thus the summit area is well resolved to ~8 km, but some of the shallow (< 2 km) anomalies on the rift zones show less resolution and significant smearing.

Data Errors

Data errors may propagate into the inversion as noise and may produce artificial velocity variations. Noisy data include bad picks and poorly determined hypocenter locations and origin times.

The HVO picks are used to define the travel time of the P wave (TT^{obs} in (1)) and are generally of high quality. The quality of the pick is indicated by a factor representing the picker's confidence in determining the start of the P wave arrival on the seismogram. The quality factor ranges from 0 to 4 where 0 indicates high confidence and 4 indicates very low confidence. The HVO picks in the data set are mostly 0's (68%) and 1's (22%), with some 2's (6%), 3's (4%) and 4's (<0.1%). Originally the inversions were done for the HVO data without any weighting of the Δt's (i.e., $w_i^t = 1.0$ for all rays). Inversions were redone with weighting for two reasons. One, to test the effect of decreasing the significance of poorly determined picks. Two, to reduce the differences between the HVO location method, which included time and distance weighting, and our original inversion which did not. Travel times in the inversion are weighted according to the quality factors, such that a quality factor of 0 is given a weight of 1.0 and the weighting is decreased by 0.25 as the quality factor increases. A quality factor of 4 is given a weight of 0.0. The resulting images are almost exactly the same as the original images with a few, very small changes in the amplitude of a few anomalies. Large amplitude anomalies were not reduced, probably because only 10% of the picks were poor enough to be significantly down-weighted in the inversion. Therefore the quality of the HVO picks does not appear to contribute much noise to the images.

Even though the picks are relatively well determined, the hypocenters and their origin times may not be. To check the accuracy of hypocenter locations and origin times, the events were relocated using HYPOINVERSE [*Klein*, 1989] and the standard HVO layered velocity model (Figure 4). Travel times were weighted using the quality factors, but in addition the relocation program applies a progressive down-

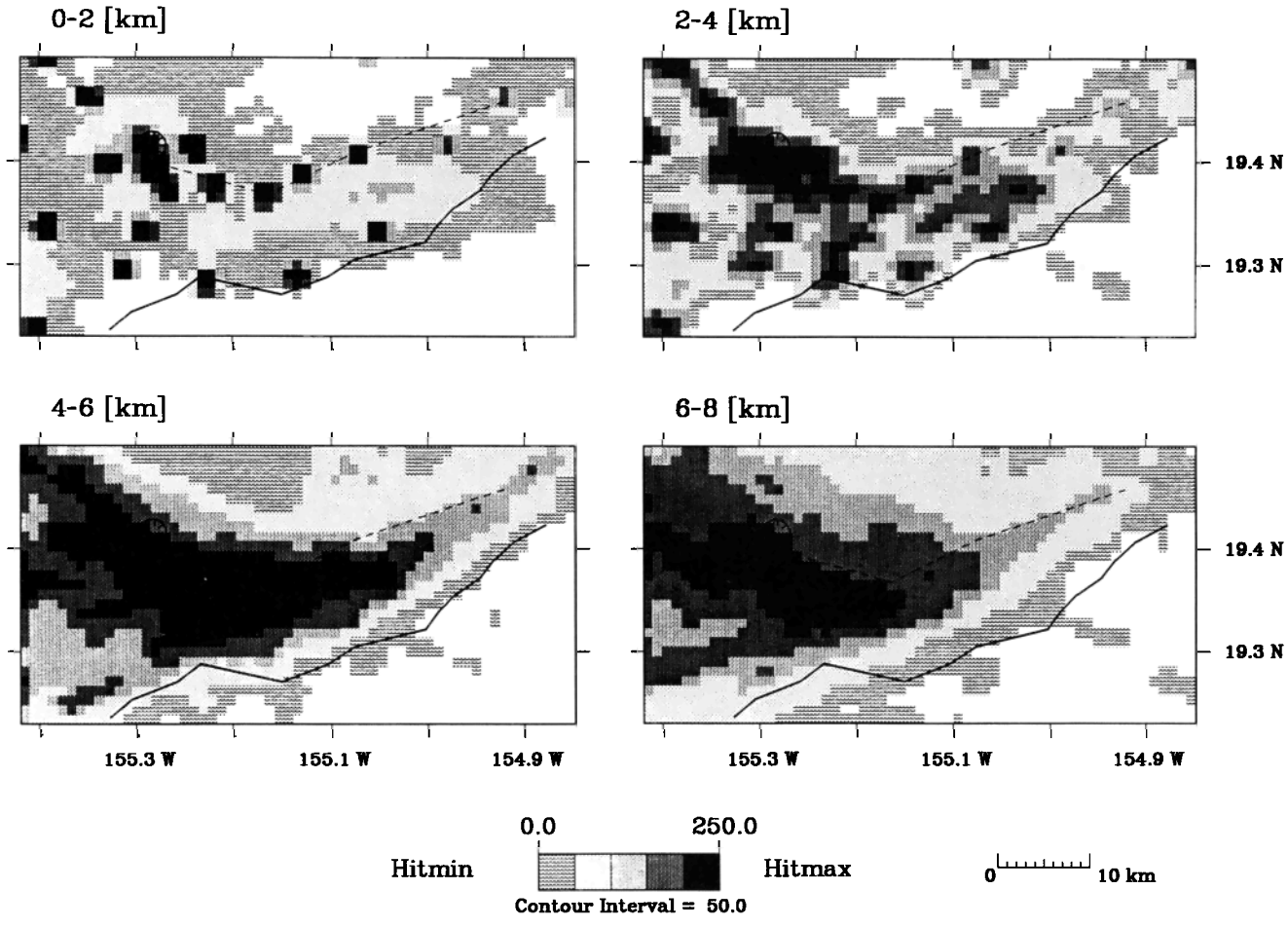

Fig. 6b. Hit count plots showing the ray coverage for the relocated hypocenters (determined using the standard layered velocity model and HYPOINVERSE [*Klein*, 1989]).

weighting of events that have large travel time residuals [see *Klein*, 1989]. Poor data are also filtered out by eliminating events or picks that cannot be fit within the error limits of the program. The average mean errors and their standard deviations for the relocated events (12,090) determined in HYPOINVERSE are: hypocenter depth = 3.58 km, horizontal distance = 1.89 km and the root mean square of the travel time residuals = 0.12 s. Station delays are not applied in the relocations because they implicitly include corrections for small-scale structures near the stations that we want to image and their exclusion does not significantly reduce relocation accuracy.

The results of the relocations (Figure 3*b*) indicate that events are shifted slightly from the locations given in the original HVO phase data (Figure 3*a*). Events from January are used to compare differences in hypocenter depth and origin time between the HVO data set and the relocated events. The mean difference in depth is 1.86 ± 2.15 km and the mean difference in origin time is 0.22 ± 0.51 s. These are the absolute values of the differences; 57% of the events are shallower than the HVO locations and 67% of the origin times are earlier than the HVO times. Many of the relocated hypocenters along the summit, ERZ and south flank are shallower, while the relocated hypocenters along the Kaoiki fault zone from 5 to 10 km depth are generally shifted deeper (Figures 3*a* and 3*b*). In terms of lateral changes, the HVO locations are shifted by <2 km. Events on the south flank, Kaoiki fault zone and LERZ tend to be shifted toward Kilauea summit, while the two shallow (< 10 km), summit clusters are less distinct after relocation (Figure 3*b*).

We have not relocated hypocenters in our three-dimensional velocity model, but *Thurber's* [1987] results indicate how significant these changes may be. The one-dimensional velocity model (similar to *Klein's*, [1981]) relocations compared to his three-dimensional velocity model relocations were more similar along the summit and USWRZ and less similar along the Kaoiki fault zone, LSWRZ and ERZ than the HVO locations compared to his three-dimensional relocations. This may be attributed to the implicit inclusion of station delays in the HVO locations and the fact that the one-dimensional velocity model is most appropriate for Kilauea summit. In fact, *Thurber* [1987] may have avoided some of the problems related to using a one-dimensional velocity model to obtain a new three-dimensional starting model for his inversion, by reinverting over only the summit area, where the one-dimensional velocity model is most appropriate, and using a smaller set of well-located events. While it is unclear that his three-dimensional images are significantly more accurate than ours, the resulting lateral velocity variations around the summit of Kilauea are similar between the two studies.

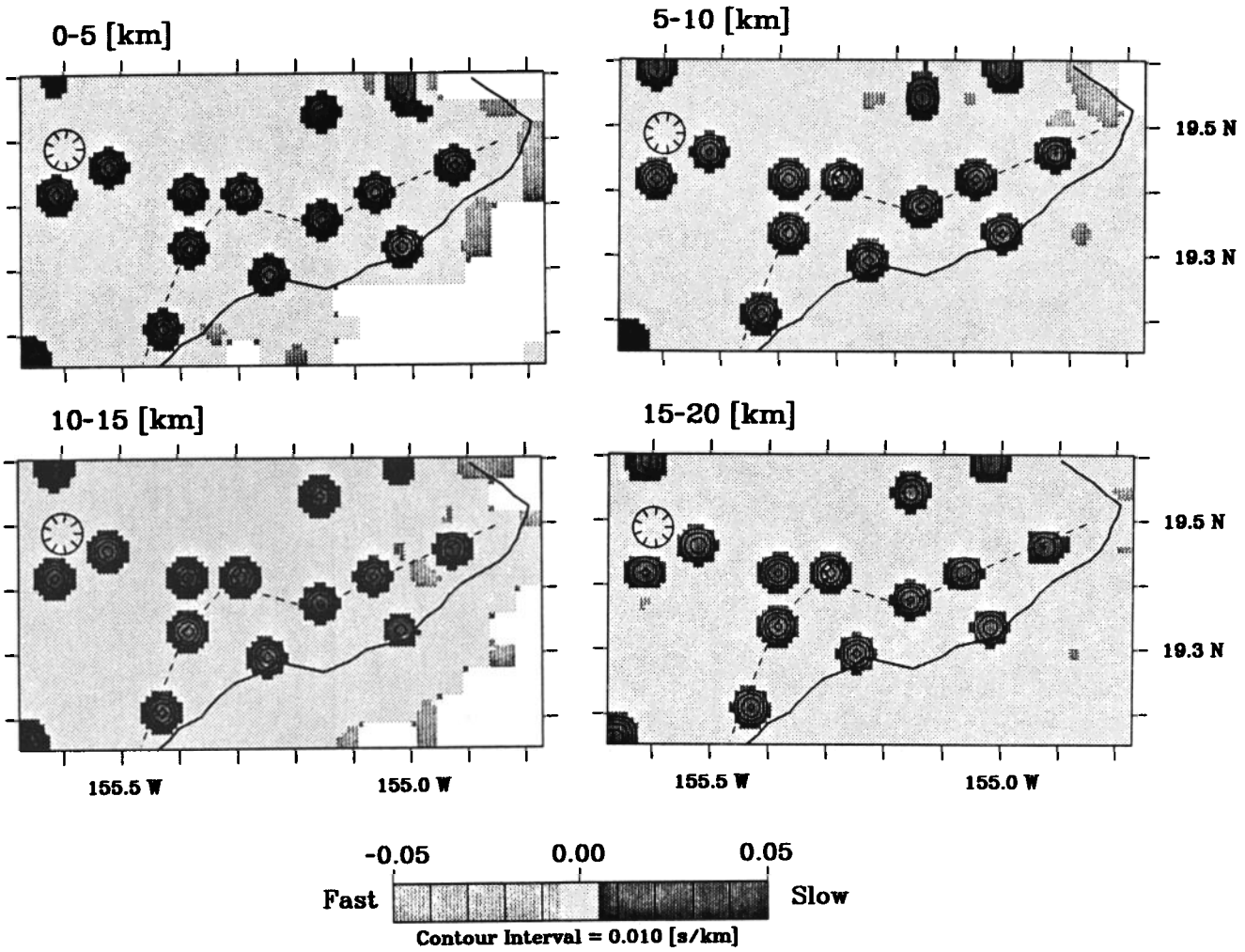

Fig. 7. Impulse tests shown in 5-km layers for the coarse model to a depth of 20 km. A slowness of 0.05 s km^{-1} was input for all the locations for each depth separately. Ray paths used are from the relocated hypocenters.

Comparing the unweighted inversion of the original HVO data (Figures 9*a* and 10*a*) with the weighted inversion of the relocated data (Figure 9*b* and 10*b*) shows the amplitude (which partially corresponds to noise) of most of the HVO anomalies are reduced in the HYPOINVERSE images. These two sets of residual slowness images also show the most significant changes in sign and shape of the anomalies compared to inversions done using only the HVO hypocenters or the relocated hypocenters. The most obvious and important difference is that the summit area is fast in the shallow layers (0–5 km, Figure 9*a* and 0–2 km, Figure 10*a*) in the images derived from the HVO data, while the summit is slow in the same shallow layers (Figures 9*b* and 10*b*) in images derived from the relocated data. Differences at the summit cannot be explained by just adding noise to the HVO data, but are due to a combination of effects including source distribution bias, station distribution bias, station delay bias, ray path bending and velocity model.

Model Errors

Model errors include the nonuniformity of the earthquake and station distribution and the inappropriateness of station delays, velocity models, ray tracing and model spaces. The amount of noise introduced into residual slowness images by various model errors is estimated through a series of tests. In some cases, these tests can isolate one source of model error associated with a "noisy" anomaly, but in most cases the inferred noise in the images comes from more than one source.

Source distribution bias refers to the clustering of hypocenters along the summit and rift zones of Kilauea (Figure 3). These clusters may artificially add signal to anomalies defined in these regions. To test this effect, we removed events in populated areas between 0–10 km depth. Events with magnitudes <1.25 were removed because this magnitude cutoff provided the most uniform spatial coverage. The resulting images showed some small decreases in the amplitude of some anomalies. Using the HVO hypocenter locations, with 4,892 low-magnitude events removed, the most significant changes in residual slowness occurred at the summit and along the ERZ. The large fast zone on the summit in Figure 10*a* decreased in amplitude, while the slow zone southeast of the summit increased in size and amplitude. The fast zone along the UERZ was significantly reduced and most of it was replaced with a low amplitude slow zone connected to the slow region southeast of the summit and the slow region at the bend in the ERZ. Therefore, the largest changes were near the summit in the shallowest layer (0–2 km) of the fine model and this is expected since

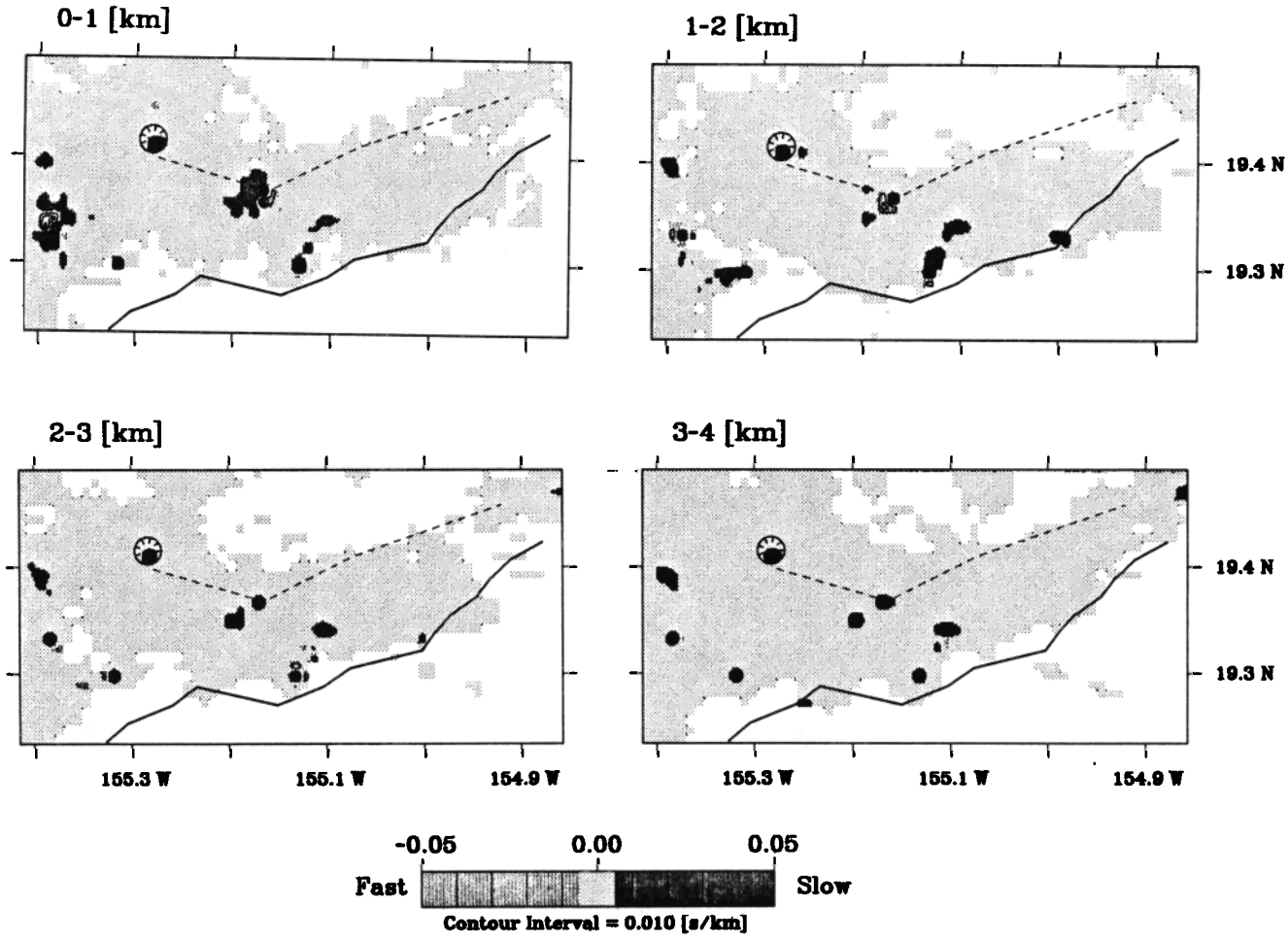

Fig. 8. Impulse test results shown in 1-km depth slices for the fine model. A slowness of 0.1 s km^{-1} was input. Ray paths used are from the relocated hypocenters.

the worst clustering occurs there (Figure 3). Unfortunately, it is hard to avoid this source distribution biasing without losing model resolution. *Thurber* [1987] noted this clustering problem in his inversion of a much smaller area, covering only the summit region with less resolution.

Station distribution and station delay biases are most obvious in the shallow layers (0–4 km) of the fine model. We have uneven hit count distribution in the shallow layers (Figure 6) because the rays must approach the stations. Comparing the slowness images (Figure 10*a*) for the inversion of the HVO data at these shallow layers with their corresponding hit count plots (Figure 6*a*) shows that about 60% of the high hit count blocks are correlated with high amplitude anomalies and most of these anomalies are slow. These anomalies may represent the local structure beneath each station (i.e., the station delay) relative to our velocity model. We want to determine these structures, but we do not want to overinterpret anomalies that are partially or completely enhanced artifacts of the station distribution. Since we cannot move or add stations to check this biasing we tried changing the one-dimensional velocity model.

Changing the velocity model allows us to look at station biases and more importantly, the appropriateness of the standard layered velocity model. We decreased the shallow layer velocities according to the velocity models of *Crosson and Koyanagi*, [1979] and *Hill and Zucca* [1987], but left the deeper velocities the same as in the original model (See Figure 4). The variation in the shallow layer velocities (> 18%) is larger than the largest velocity variation (14%) caused by the highest amplitude slow anomaly (~ 0.5 s km^{-1}) in the 0–2 km depth of Figure 10*a*. The events were relocated using this modified velocity model in HYPOINVERSE and the inversion was done using the same parameters as before (i.e., same damping factor and same weighting scheme). Comparing the shallow layers (0–2 km) in Figures 10*b* and 10*c* we note a decrease in the amplitude of slow anomalies and an increase in the amplitude of fast anomalies along the south flank and the upper and middle ERZ in Figure 10*c*. We believe these differences are caused by changing the velocity model and do not reflect station distribution bias. There are two areas in the 0–2 km depth that are different between the inversions and may be artifacts of the station distribution. The two slow anomalies near Mauna Iki and Kilauea Iki are significantly reduced in signal by changing the velocity model, while the other slow features along the summit and ERZ are not dramatically reduced (Figure 10*c*). This suggests that station distribution and clustering of ray paths to Mauna Iki and Kilauea Iki stations has artificially enhanced the signal in these two regions. Given the instability of these two slow anomalies, they may not be related to the structural character of these areas.

The appropriateness of the model space was checked by

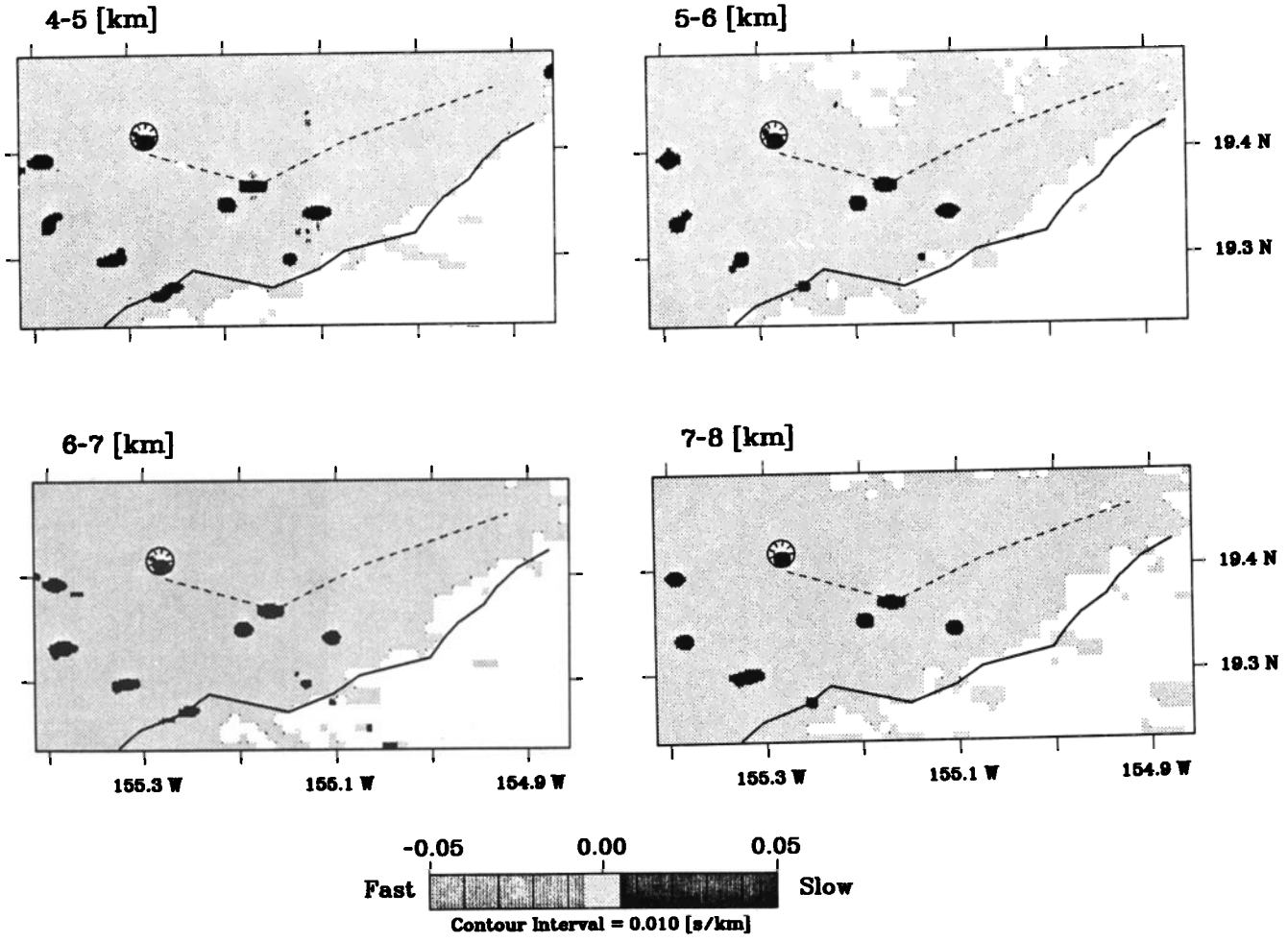

Fig. 8. (continued)

shifting the model grids by one half their cell size and by using different cell sizes (3x3x3 km and 4x4x4 km). Shifting the model grids did not change the slowness images although the shape of some of the anomalies varied. Using different cell sizes did not change the slowness images either and given that the resolution tests indicate anomalies can be resolved using the smaller cell size of the fine model we have shown these results in this paper. So, in general, the model spaces chosen for the inversion are reasonable and do not add any significant biasing to the inversion.

The approximate ray tracing technique (ART) can only approximate the real path so it is important to estimate the effect of slightly different ray paths on the images. Two sets of slightly different ray paths and travel times were obtained for hypocenters from events in January. For one set, hypocenters were relocated and inverted with travel time residual weighting applied in both steps. For the second set, hypocenters were relocated and inverted without weighting applied in either step. The weighted ray paths tended to be more concentrated near the summit and at shallower levels, while the unweighted ray paths were more dispersed, traveling to the stations from a greater distance. Tighter clustering of events for the weighted case may add a small source distribution bias, while the longer ray paths for the unweighted case may reduce the travel time residual by distributing it over a longer ray segment, thus offsetting the larger errors in this case. The resulting images for the two cases are very similar suggesting that small differences in ray paths do not significantly effect the images. Therefore more accurate locations and "more accurate" ray paths can account for small changes in the size and shape of anomalies, but do not really change the sign (i.e., fast or slow) of the signal.

Although small changes in ray paths do not effect the resulting images, ray bending may not have such a subtle effect. The ART models straight line segments and cannot model rays that bend or curve around a large velocity variation. Ray paths around the summit of Kilauea at a shallow level (i.e., where the magma reservoir is inferred) may be significantly affected by the bending of these rays around a magma chamber through much faster intrusive dikes. Some important changes in the residual slowness anomalies for the fine model (Figure 10) in the shallow summit region may be partly due to this effect but only a more complete inversion with a three-dimensional velocity model and the appropriate ray tracing technique can address this issue.

Returning to the original inversion using the HVO data, the large, high amplitude fast region on the summit in the fine model (0–2 km, Figure 10*a*) is partly an artifact of source distribution, station distribution and station delays. Unfortunately, because of its size and location it may be covering and averaging out slow anomalies that are imaged in

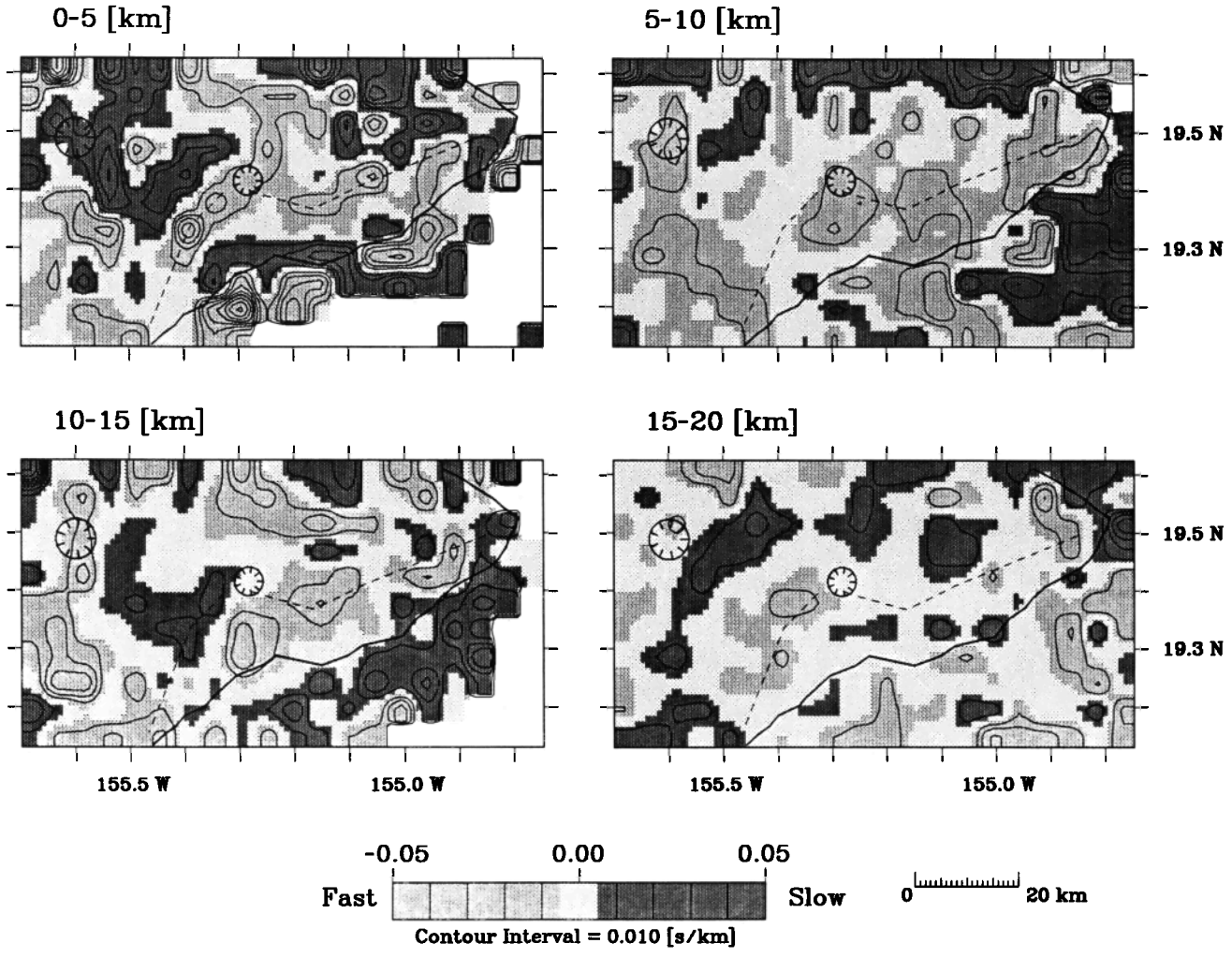

Fig. 9a. Slowness residual plots for the HVO hypocenters for the coarse model in 5-km depth slices. The dark shaded areas represent slow velocity zones while the lighter shades represent fast velocity zones.

the inversions using relocated hypocenters. This fast zone may also be partially due to the one-dimensional approximate ray tracing technique that cannot account for rays bending around a shallow reservoir between two sharp velocity discontinuities. Given these important concerns about the stability of the summit anomalies, we have chosen to interpret the shallow summit (0–4 km) as fast just north and northwest of the summit and slow just southeast of the summit.

RESULTS AND DISCUSSION

The residual slowness images derived from the tomographic inversions are consistent with current models of Kilauea's conduit plumbing system and provide important insight into some of the small-scale structures that are poorly defined by previous workers [*Ellsworth and Koyanagi*, 1977; *Crosson and Koyanagi*, 1979; *Ryan et al.*, 1981; *Thurber*, 1984; *Hill and Zucca*, 1987]. The results show detailed lateral heterogeneities and define structures in aseismic zones not covered by geophysical studies using only seismicity patterns [*Ryan et al.*, 1981]. *Hill and Zucca* [1987] summarized the range of *P* wave velocities expected from different Hawaiian rocks and using their table [*Hill and Zucca*, 1987, Table 37.2] as a guide, "interpretations" of velocity anomalies in the residual slowness images (Figures 9 and 10) have been inferred. In general, a slow velocity may correspond to weaker, porous, subaerial lava, an area with large fractures or an area with a high fluid to rock ratio (e.g., magma or partial melt). A fast velocity may correspond to dense intrusive bodies, buried pillow basalts or possibly cumulate material. The features described below are mainly robust anomalies related to the subsurface structure of Kilauea and are not artifacts of noise in the data or the propagation of noisy data in the model. The following discussion summarizes the main structures inferred from the residual slowness images in the six major tectonic zones of Kilauea and compares the tomographic results to previous geophysical models.

Kilauea Summit

The coarse model (Figure 9) averages much of the significant small-scale structure of the shallow summit reservoir, but may define the extent of the vertical conduit. From 5 to 10 km depth, there is a fast zone centered due south of the summit that may represent part of the main vertical passageway for Kilauea's magma supply. *Ryan et al.* [1981] inferred a primary, elliptical-shaped conduit just southeast of Halemaumau extending from a depth of 6.5–14.6 km. Their

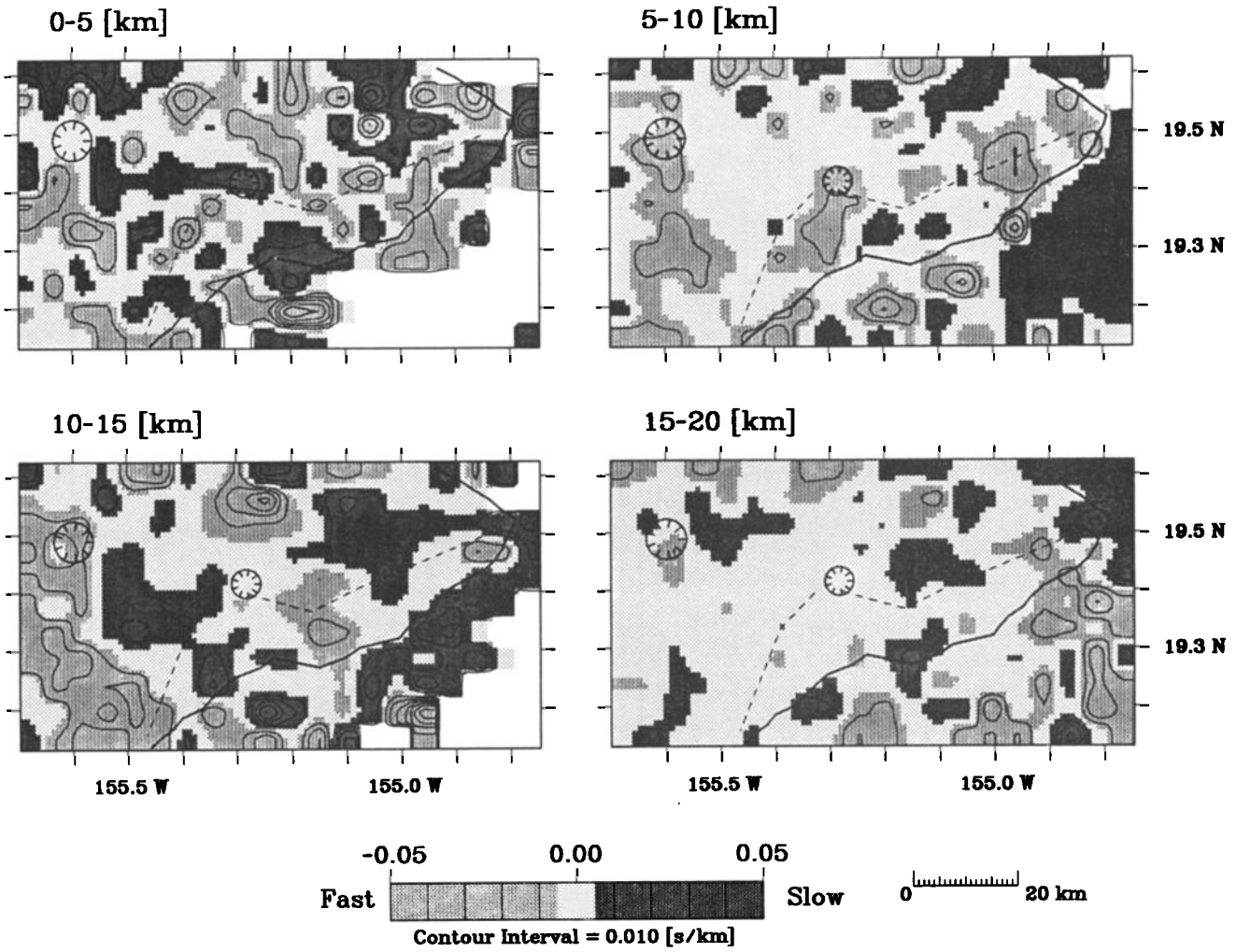

Fig. 9b. Slowness residual plots for the relocated hypocenters for the coarse model in 5-km depth slices.

conduit flares out to the south with depth. The fast region in our inversion is shorter, extending to ~10 km depth. More recent studies are consistent with a shorter conduit. *Hill and Zucca* [1987] described the main conduit as a sheeted, dike-like complex widening to the south until a depth of ~9 km. *Thurber* [1984 and 1987] also found a similar southward shift of the high velocity conduit with increasing depth to 8 km. *Delaney et al.* [1990] used the relatively steady, long term ground deformation data from Kilauea to suggest an extensive vertical conduit system to at least 9 km.

The cross sectional area of the fast region beneath the summit is larger than *Ryan et al.'s* [1981] inferred conduit and probably includes some structural information about the south flank. The high velocity region is in the same general location as a cluster of seismicity centered beneath the south flank from 5 to 10 km depth in *Klein et al.'s* [1987, Figure 43.18A] summary of Kilauea's seismicity. Klein et al.'s cross section is a little misleading because most of the earthquakes in this cluster define a linear zone just east of Halemaumau on the south flank in plan view. In fact, the fast zone (Figure 9) is centered where there is a lack of seismicity (Figure 3). Therefore part of the fast zone may be related to a relatively consolidated, mobile block separated from similar blocks by lines of breakage [*Ryan*, 1988] such as Klein et al.'s linear cluster. Furthermore, this high velocity region may be easily distinguished because it overlies a low velocity layer of oceanic sediments inferred to lie just beneath this zone of seismicity [*Crosson and Koyanagi*, 1979; *Furumoto and Kovach*, 1979; *Crosson and Endo*, 1982; *Li et al.*, 1992].

The fine model (Figure 10) provides more detail of the shallow reservoir and conduit structure to a depth of 8 km. From 0 to 2 km, a concentrated, high amplitude fast zone is centered north of the summit. This high velocity region probably represents a partial wall and/or cap of dense intrusive material surrounding and bounding the magma reservoir on its north side. Such a fast zone has been suggested by *Ryan et al.* [1981], who modeled an elliptical magma chamber crown at a depth of 1.1–1.9 km. *Thurber* [1984, 1987] also inferred a roof to the shallow reservoir from a high velocity region imaged just north of the summit extending to ~2 km depth.

Slightly southeast of the summit, a slow zone extending away from the summit (Figures 10*b* and 10*c*) may represent the shallow magma reservoir. The summit reservoir is poorly defined in Figure 10*a* because the lower velocities are overwhelmed by the high velocity anomaly to the north. Previous workers have modeled a shallow reservoir

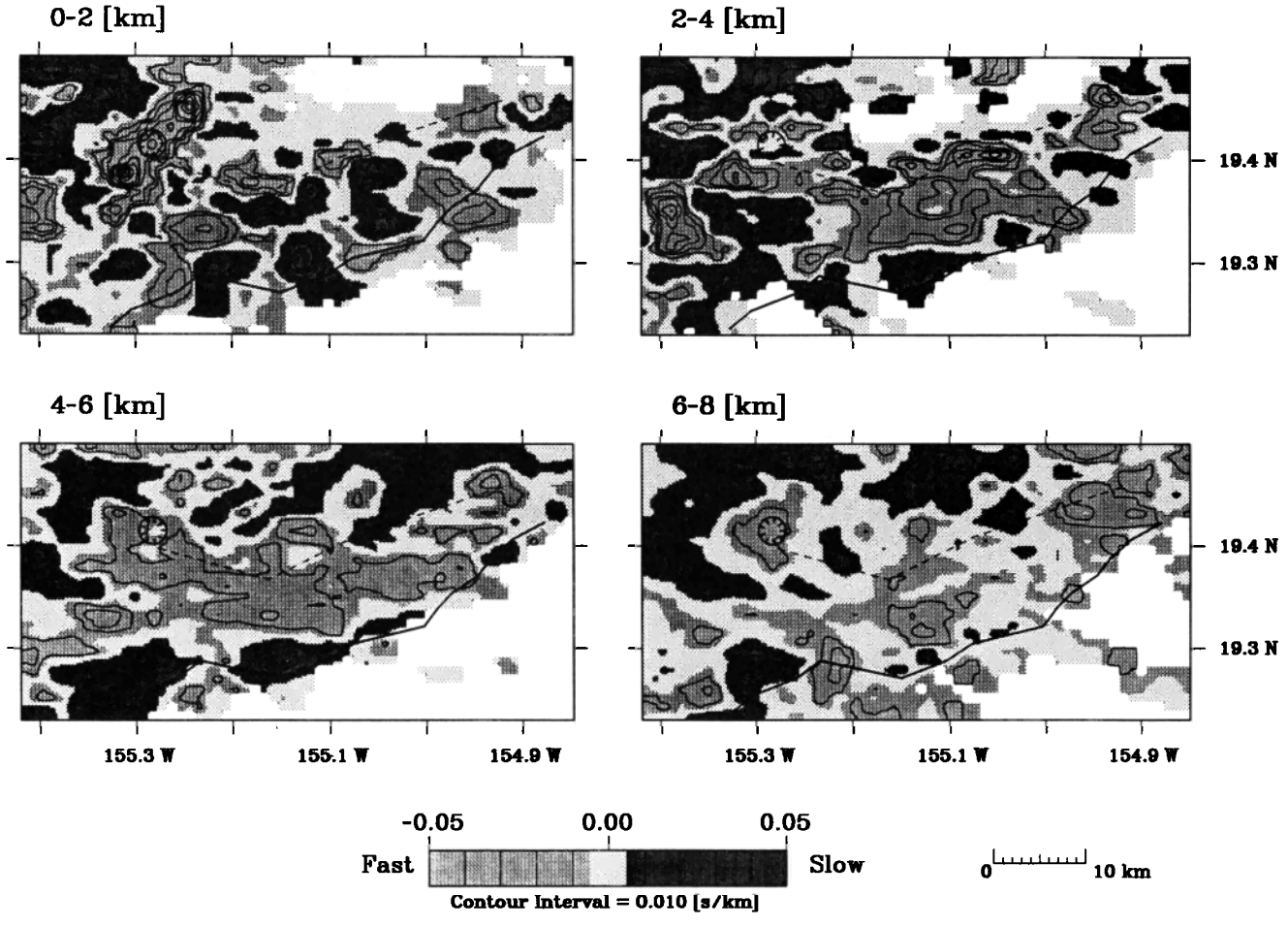

Fig. 10a. Slowness residual plots for the HVO hypocenters for the fine model in 2-km depth slices.

at approximately 2–4 km depth southeast of the summit [*Ryan et al.*, 1981; *Thurber*, 1984, 1987; P. Ho-Liu et al., preprint, 1991]. *Thurber* [1984, 1987] imaged a localized, low-velocity zone from 1.5–2.5 km. Many workers have suggested that the shallow magma reservoir of Kilauea is a laterally elongate, planar, compartmentalized body of dikes and sills rather than a simple, spherical magma chamber [*Fiske and Kinoshita*, 1969; *Swanson et al.*, 1976; *Ryan et al.*, 1981; *Duffield et al.*, 1982; *Wilson and Head*, 1988]. The residual slowness images complement these models since the slow zone is laterally extensive to the southeast but is surrounded by fast regions.

In the next depth level (2–4 km) the summit is slightly fast north of the caldera and slightly slow south of the caldera. These anomalies are remnants of the stronger anomalies in the shallower layer and probably do not extend to a depth of 4 km. Therefore the magma chamber beneath Kilauea is inferred to be a laterally extensive, southeastward trending zone of partial melt centered ~2 km south of Halemaumau crater at a depth of 0–3 km.

Rift Zones

ERZ. In the coarse model (Figure 9), the ERZ has two distinct fast anomalies along its surface trace near Makaopuhi and Kalalua Cone in the shallowest layer (0–5 km). The intensity of the anomaly near Kalalua suggests a high concentration of intrusive dikes and it may be a transient magma barrier as *Klein et al.* [1987] have inferred. The depth to which the rift zones extend as structural entities is questionable. The images indicate that the ERZ may extend as deep as 15 km as a discontinuous high velocity region. *Ryan* [1988] used a finite element model to infer melt-filled rift zones from 6 to 10 km, supplied with picritic magmas (i.e., cumulate-rich mush) along the boundary with the oceanic crust while *Delaney et al.* [1990] indicated a dike-like structure for the rifts to 9 km depth.

The ERZ has a high velocity signal to at least 6 km depth, which is broken up by slow features in the fine model (Figure 10). We believe these slow anomalies are due mainly to magmatic activity but other structures may explain the low velocities (e.g., cracks, rifts, weathering, temperature variations or porosity). We prefer to interpret these slow velocities as zones of partial melts because there is strong evidence (described below) for concentrated magma pockets and very little evidence for significant, anomalous zones of high porosity basaltic rock or regions along the upper parts of the rifts that contain a greater density of cracks and fractures. The one exception is the Great Crack along the LSWRZ which is poorly delineated in the shallow layer of the coarse model by any significant velocity anomaly, although it is slightly slow in Figure 9*b*.

The fine model suggests small magma reservoirs at shallow levels (0–2 km) beneath Mauna Ulu, Makaopuhi and

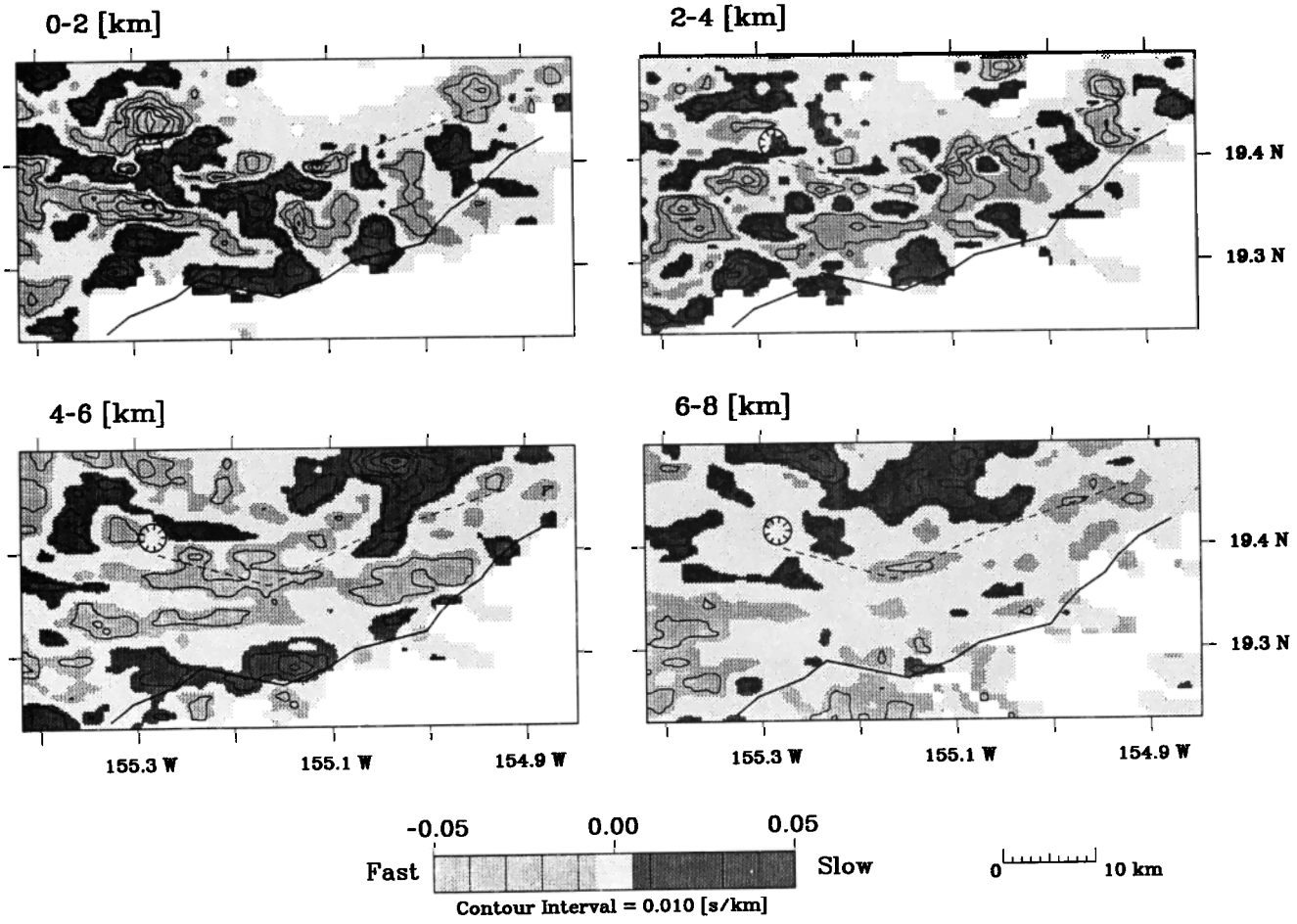

Fig. 10b. Slowness residual plots for the relocated hypocenters for the fine model in 2-km depth slices.

Puu Oo. The large amplitude slow region extending from Mauna Ulu to Puu Oo is most likely related to magma storage for the current eruption, which has been active since 1983, and past, relatively voluminous eruptions at Mauna Ulu and Makaopuhi. Extensive slow regions and lack of significant fast regions, suggest a relatively open conduit system along the UERZ at shallow levels. Previous workers have suggested a similar structural model from a variety of geophysical studies [*Eaton and Murata*, 1960; *Jackson et al.*, 1975; *Swanson et al.*, 1976; *Ryan et al.*, 1981; *Decker*, 1987; *Klein et al.*, 1987; *Hoffmann et al.*, 1990; P. Ho-Liu et al., preprint, 1991]. P. Ho-Liu et al. found attenuating anomalies at Mauna Ulu and Puu Oo using seismic data from 1986, supporting our suggestion of shallow magma pockets. *Klein et al.* [1987] indicated magma zones near the summit, at Makaopuhi and along a region between Puu Kamoamoa and Kalalua. The inferred magma pocket under Mauna Ulu and Makaopuhi may be a more long-lived storage zone present before the Mauna Ulu eruptions of 1968–1971. *Jackson et al.* [1975] and *Swanson et al.* [1976] used geodetic and petrographic information to suggest a shallow magma reservoir beneath Makaopuhi Crater before the 1968 and 1969 eruptions. Their evidence included many shallow earthquakes (<5 km), uplift of the area and the eruption of hybrid and differentiated lavas which indicated prolonged storage before extrusion. The idea of a long-lived magma pocket near the bend in the ERZ is consistent with the seismic and geodetic history of Kilauea. Using the magma supply rate, 0.1 km^3yr^{-1} [*Swanson*, 1972; *Dzurisin et al.*, 1984] and the estimated volume of the magma reservoir, 11 km^3 [*Wright*, 1984] the average residence time for magma is 100 - 120 years [*Decker*, 1987]. Therefore some of the anomalies in the images may be due to long term magma storage zones along the ERZ that probably receive new injections of magma from the hotspot source.

At Kalalua, just east of the slow region, the fast area in the fine model (0–2 km) may represent an intrusive barrier to magma migration in the ERZ conduit. From 2 to 4 km the ERZ is generally fast and the southward spreading of these fast regions suggests intrusive diking along the ERZ widens with depth. The fast regions at Kalalua and Kaliu probably represent a zone of dense intrusives acting to impede magma migration at this level. *Klein et al.*, [1987] indicated that intrusion of magma beyond these barriers is rare. Except for 1955 and 1960, most of the recent eruptive activity on Kilauea has been confined to the upper and middle east rift zone, west of Kalalua [*Dzurisin et al.*, 1984; *Decker*, 1987]. In fact, there have only been 2 out of 30 seismicity-related rift zone injections into the LERZ since the 1975 Kalapana earthquake [*Decker*, 1987].

SWRZ. The southwest rift zone in the coarse model (Figure 9, 0–5 km) is fast along its surface trace to near Mauna Iki. The fast region at the bend has a very high amplitude, indicating a relatively more concentrated zone of in-

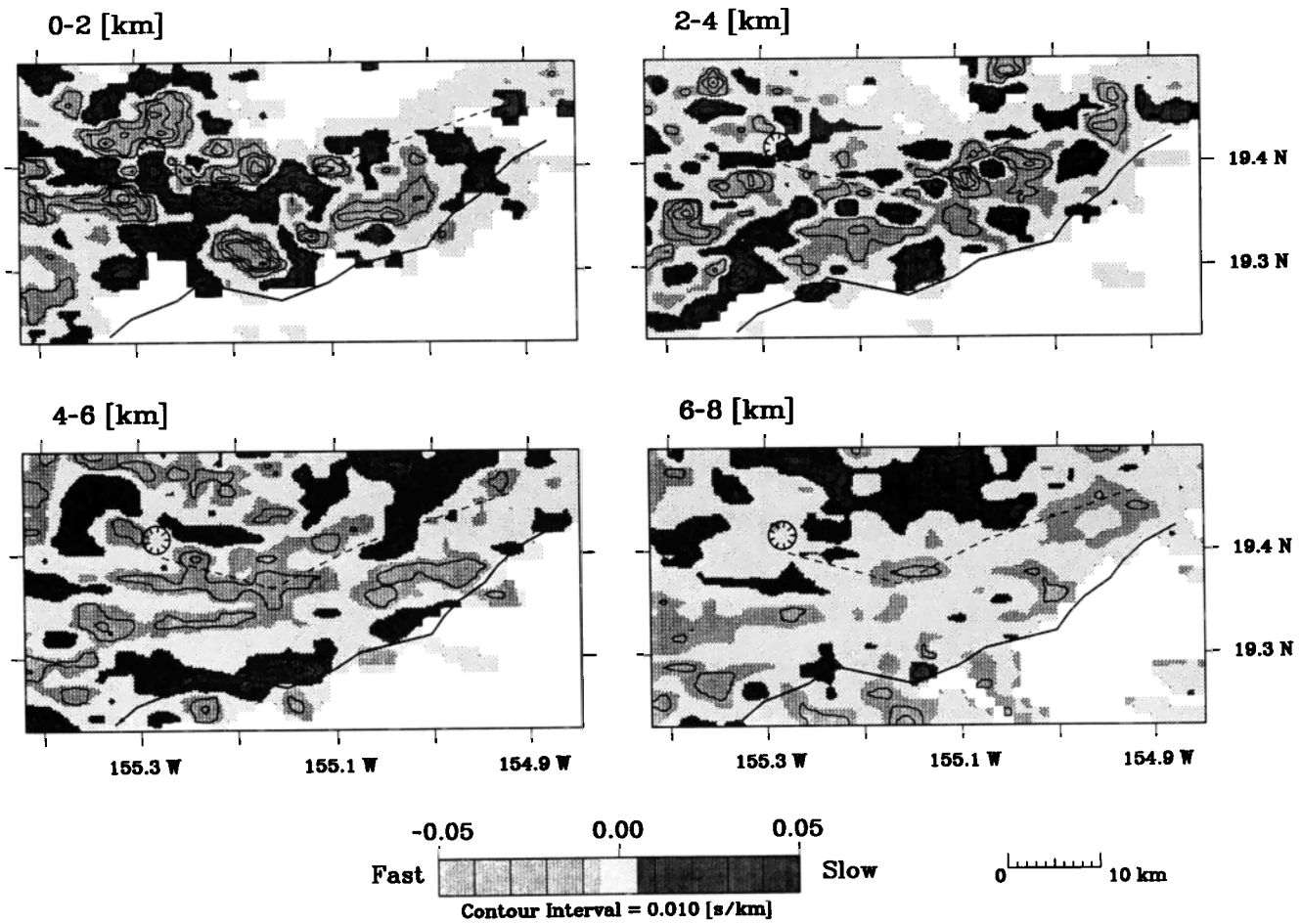

Fig. 10c. Slowness residual plots for the relocated hypocenters determined using the modified layered velocity model (slower shallow velocities) for the fine model in 2-km depth slices.

trusives acting as a barrier to magma propagation [*Klein et al.*, 1987]. The presence of this feature at the bend is probably not a coincidence, but is related to increased stresses introduced by the change in structural character and direction of the rift and the rift's proximity to Mauna Loa. The lower SWRZ is average (Figure 9*a*) to slow (Figure 9*b*) possibly due to the presence of the Great Crack, a large grabenlike structure whose tensional rifts would tend to reduce velocities of rays traveling perpendicular to the cracks. From 10 to 15 km, the trace of the SWRZ is partially covered by a slightly slow zone paralleling the surface trace of the rift. This slow anomaly is similar to the attenuating anomaly imaged by P. Ho-Liu et al. (preprint, 1991) along the same region. Although we cannot explain this anomaly, we believe the seismic velocities are slightly slower than average in this area and more work is needed to determine the structural character of this region.

The SWRZ shows a similar overall pattern as the ERZ in the fine model (Figures 10*a* and 10*b*). The rift is fast and the high velocity begins to diffuse below ~6 km. There are some slow patches that break up the fast regions but most of these anomalies are not robust between the different inversions. From 2 to 4 km depth, there are two large fast zones, one very close to the summit and the other near Mauna Iki, that are probably related to intrusives. These structures may act as barriers to eruptions or intrusions along the SWRZ. *Klein et al.* [1987] defined Mauna Iki as a major barrier to magma migration and our images suggest this barrier is within 2–4 km depth.

Deep Structure of Rifts. The deep structure of the rift zones is controversial because ground deformation studies, gravity data and refraction surveys cannot produce unique models. The residual slowness images have both fast and slow anomalies beneath the rifts related to the rift conduits structural complexity. It is generally agreed that dikes are intruded either vertically or steeply southward dipping and they tend to have tapered, blade-like ends because of the stresses placed on the dike tips [*Fiske and Jackson*, 1972; *Swanson et al.*, 1976; *Rubin and Pollard*, 1987; *Dieterich*, 1988]. The geometry and growth of the dike complex is problematic. *Swanson et al.* [1976] agreed with *Kinoshita et al.'s* [1963] interpretation of the dike complex having a shallowly dipping north flank and a steeply dipping south flank. They suggested the growing dike complex moves southward and intrudes younger dikes, on average, at a higher elevation, thus producing a steep south side to the complex [*Swanson et al.*, 1976, Figure 19]. This geometry was modified by later workers whose data suggest a shallowly dipping south side of the rift complex [*Crosson and Endo*, 1982; *Thurber*, 1984; *Hill and Zucca*, 1987]. The south side may have a shallower dip, if vertical dikes are pushed southward as more dikes are intruded at the active crest and these dikes become buried

by new lava flows from the topographically higher rift conduit as the ERZ grows [*Hill and Zucca*, 1987, Figure 37.12]. Thus, after a period of growth, the rifts have a triangular high velocity core. Our slowness images show a more asymmetric southward widening of the fast regions along the ERZ with almost no fast anomalies north of the rift. This suggests a more complicated, nonuniform growth of the rift with a greater build-up of intrusive dikes on the south side of the rift.

Fault Systems

The Hilina fault system is imaged as slow regions to ~6 km. In the coarse model (0–5 km) there are coastal slow zones at 155.34°W along the Hilina Pali, at 155.12°W along the Holei Pali and at 155.05°W south of Kalalua, on the eastern segment of the Hilina fault system. These coastal slow anomalies are also seen in the fine model from 0 to 6 km and correlate with the attenuating anomalies from 0 to 6 km imaged by P. Ho-Liu et al. (preprint, 1991). These low velocity features are probably due to the subaerial lava flows and fractures created by the normal faults of the Hilina System. In general, slow velocities and high attenuation are associated with faulting. Many workers have indicated that the Hilina faults are very shallow features, extending only into Kilauea's hyaloclastic layer, from 1 to 3 km depth [*Moore and Fiske*, 1969; *Swanson et al.*, 1976; *Crosson and Endo*, 1982; *Hill and Zucca*, 1987]. The slow anomalies extend deeper than 3 km indicating the Hilina faults may be deeper.

The Koae fault system is indistinguishable in the coarse model, but some of its structural complexity can be deciphered in the fine model (Figure 10). In the shallowest layer, 0–2 km, the northeastern end of the Koae is slow. In Figure 10*a*, the slow anomaly is isolated, while in Figure 10*b* the slow anomaly is connected to our inferred shallow reservoir slow anomaly. The evidence for an open, direct connection between the summit reservoir and the Koae fault system is inconclusive. Our preferred "interpretation" of the slow anomalies in Figure 10*b* is that these slow regions are not connected and have just smeared into one another due to smoothing and contouring. The rest of the Koae (southwestern three-fourths of the fault system) in the shallow layer, 0–2 km, is fast. In the next depth slice (2–4 km), the fault's surface trace has an average velocity bounded by the fast anomaly related to a SWRZ intrusive barrier to the north and a slow anomaly to the south that is possibly related to the subaerial basaltic flows on the south flank (Figure 10*b*). From 4 to 6 km the Koae is part of the high velocity region related to dike intrusions along the rifts. The Koae is a difficult fault zone to interpret from the images and its complicated history. It is an extensional fault system to approximately 10 km [*Duffield*, 1975], but because it is connected to the rift zones it is also a zone of intrusive diking [*Yang et al.*, 1992; *Klein et al.*, 1987; *Thurber*, 1987; *Ellsworth and Koyanagi*, 1977; *Swanson et al.*, 1976] and rare eruptions [*Duffield*, 1975]. The Koae may be an ancient caldera-rift system of Kilauea [*Holcomb*, 1987; *Duffield*, 1975] and its development may be directly related to the forceful intrusion of magma, like the current rift system. *Thurber* [1984 and 1987] and *Ellsworth and Koyanagi* [1977] imaged the Koae as a high velocity region in their inversions. *Yang et al.* [1992] re-examined geodetic data and modeled many dike intrusions along the Koae to a maximum depth of 9 km. They defined a zone of intrusion (i.e., "South Intrusion Dike Zone") from the summit southward toward the Koae and then intruding southwestward along the Koae fault zone to 5 km depth which is consistent with the fast anomalies in our images. The shallow slow anomaly along the northeast end of the Koae may be related to tensional cracks or possibly a small zone of partial melt. *Swanson et al.* [1976] noted that dilation along the Koae increased to the east and *Thurber* [1987] noted that focal mechanisms of earthquakes at deeper depths (4–8 km) indicated north-south tension on the eastern Koae and north-south compression on the western Koae. There is also more melt currently being supplied and stored along the UERZ than the SWRZ [*Duffield et al.*, 1982] and *Klein et al.*, [1987] have distinguished a "transition region" between the ERZ and the Koae fault zone where in 1973 magma intruded uprift. So a small zone of magma storage at the intersection of the Koae and the ERZ is a plausible cause for slow velocities.

The shallow Kaoiki fault system (0–5 km depth, Figure 9) has slow to average velocity anomalies in the coarse model possibly related to shallow tensional structures defined along the surface of the fault zone. Southeast facing en-echelon sets of normal faults may have performed the same structural function for Mauna Loa as the Hilina fault system currently performs for Kilauea [*Lipman*, 1980]. From 10 to 15 km depth, the Kaoiki has a slightly slow anomaly, which also covers part of the SWRZ, but as discussed earlier we do not have a structural interpretation for this small deviation in the average velocity. If the Kaoiki intersects the SWRZ near its boundary with the oceanic crust [*Swanson et al.*; 1976] the velocities might be slowed down, but this cannot be determined without more work.

CONCLUSIONS

Travel time tomography provides detailed images of the lateral heterogeneity of Kilauea. Using a dense seismograph network and a large number of local events allowed excellent ray coverage of the six major structural entities of the edifice. Resolution and error analyses provided a semi-quantitative method for determining which features are questionable and poorly constrained.

The model suggests a shallow (0–2 km) magma reservoir centered 2 km southeast of Halemaumau caldera, with a plexus of discontinuous open tubes extending to 6 km. This primary conduit and shallow storage area is surrounded by high velocity anomalies representing dense intrusives that form containment boundaries for the reservoir. The rift zones are distinguished by high velocity dike complexes that widen southward to 6 km depth. On a finer-scale the rift zones are more intricate, being strong enough to support a constructional ridge on the surface and weak enough to allow the concentration and intrusion of magma in the subsurface. Small magma pockets are inferred beneath Mauna Ulu, Makaopuhi and Puu Oo on the ERZ.

Intrusive barriers are inferred at Kalalua and Kaliu at shallow levels along the ERZ because of high velocity anomalies in the images. These results are consistent with the lack of significant eruptions or intrusions along the lower ERZ since 1975 [*Decker*, 1987; *Klein et al.*, 1987]. An intrusive barrier is also inferred beneath Mauna Iki on the SWRZ, consistent with the seismicity study of *Klein et al.* [1987]. The Koae fault system is mainly imaged as a high velocity region related to dike intrusion from the rift zones. The

shallow Kaoiki (< 5 km depth) is slow, related to cracks and fractures along its normal faults. The Hilina is imaged as slow to about 6 km due to open fractures and scarps in young subaerial basalts.

Continued work on many aspects of these results would prove useful for refining the three-dimensional structure and dynamics of Kilauea. Inverting data from different time periods, particularly those reflecting the greatest contrast in the eruptive nature of Kilauea, may help define temporal variations in the volcanic subsurface. Details of transient structures from past eruptions would be useful for understanding not only the growth of the tectonic environment of the volcano, but for understanding the origin and differentiation of Hawaiian basalts. This model also lends itself to comparisons with heat flow models that define the sizes and cooling times of magma reservoirs beneath Kilauea. Therefore the velocity anomalies defined by this study should be viewed as a template to be refined and compared with other physical models of a very active, well studied volcano, Kilauea.

Acknowledgments. We would like to thank Phyllis Ho-Liu and Hua-Wei Zhou for their help and advice throughout this project. We appreciate the reviews and useful comments on the manuscript from Jim Westphal and Hiroo Kanamori. We appreciate the patient and critical reviews by two anonymous reviewers and Stuart Sipkin. We would also like to thank Carl Johnson, Bob Koyanagi and Paul Okubo for providing us with the data set for 1986 and some useful discussions on our interpretations of the tomographic images. The first author would like to add a special thanks to Robert P. Sharp for including me on a field trip to the Big Island so I could see and understand the dynamic beauty of Kilauea Volcano at least on the surface. This work was partially supported by the contracts USGS 14-08-0001-G1774 and by EAR-83-511371. Contribution No. 4942 from Division of Geological and Planetary Sciences, Caltech.

REFERENCES

Casadevall, T. J., and D. Dzurisin, Intrusive rocks of Kilauea Caldera, *U.S. Geol. Surv. Prof. Pap., 1350,* 377-394, 1987.

Clayton, R. W., and R. P. Comer, A tomographic analysis of mantle heterogeneities from body wave travel times, *Eos, Trans. AGU, 64,* 776, 1983.

Crosson, R. S., and R. Y. Koyanagi, Three-dimensional crust and mantle structure of Kilauea Volcano, Hawaii, *J. Geophys. Res., 84,* 2331-2342, 1979.

Crosson, R. S., and E. T. Endo, Focal mechanisms and locations of earthquakes in the vicinity of the 1975 Kalapana earthquake aftershock zone 1970-1979: Implications for tectonics of the south flank of Kilauea Volcano, Island of Hawaii, *Tectonics, 1,* 495-542, 1982.

Decker, R. W., Dynamics of Hawaiian volcanoes: An overview, *U.S. Geol. Surv. Prof. Pap., 1350,* 997-1018, 1987.

Delaney, P. T., R. S. Fiske, A. Miklius, A. T. Okamura and M. K. Sako, Deep magma body beneath the summit and rift zones of Kilauea Volcano, Hawaii, *Science, 247,* 1311-1316, 1990.

Dieterich, J. H., Growth and persistence of Hawaiian volcanic rift zones, *J. Geophys. Res., 93,* 4258-4270, 1988.

Dieterich, J. H., and R. W. Decker, Finite element modeling of surface deformation associated with volcanism, *J. Geophys. Res., 80,* 4094-4102, 1975.

Duffield, W. A., Structure and origin of the Koae fault system, Kilauea Volcano, Hawaii, *U.S. Geol. Surv. Prof. Pap., 856,* 1-12, 1975.

Duffield, W. A., R. L. Christiansen, R. Y. Koyanagi and D. W. Peterson, Storage, migration and eruption of magma at Kilauea Volcano, Hawaii, 1971–1972, *J. Volcanol. Geotherm. Res., 13,* 273-307, 1982.

Dzurisin, D. R. Y. Koyanagi and T. T. English, Magma supply and storage at Kilauea Volcano, Hawaii, 1956-1983, *J. Volcanol. Geotherm. Res., 21,* 177-206, 1984.

Dvorak, J. J., A. T. Okamura and J. H. Dieterich, Analysis of surface deformation data, Kilauea Volcano, Hawaii: October 1966 to September 1970, *J. Geophys. Res., 88,* 9295 – 9304, 1983.

Dvorak, J. J., A. T. Okamura, T. T. English, R. Y. Koyanagi, J. S. Nakata, M. K. Sako, W. T. Tanagawa and K. M. Yamashita, Mechanical response of the south flank of Kilauea Volcano, Hawaii to intrusive events along the rift systems, *Tectonophysics, 124,* 193-209, 1986.

Eaton, J. P., Crustal structure and volcanism in Hawaii, *Am. Geophys. Soc. Mon. 6,* 13-29, 1962.

Eaton, J. P., and K. J. Murata, How volcanoes grow, *Science, 132,* 925-938, 1960.

Eissler, H. K., and H. Kanamori, A single-force model for the 1975 Kalapana, Hawaii, earthquake, *J. Geophys. Res., 92,* 4827-4836, 1987.

Ellsworth, W. L., and R. Y. Koyanagi, Three-dimensional crust and mantle structure of Kilauea Volcano, Hawaii, *J. Geophys. Res., 82,* 5379-5394, 1977.

Fiske, R. S., and E. D. Jackson, Orientation and growth of Hawaiian volcanic rifts: The effect of regional structure and gravitational stresses, *Proc. R. Soc. London, 329,* 299-326, 1972.

Fiske, R. S., and W. K. Kinoshita, Inflation of Kilauea Volcano prior to the 1967-68 eruption, *Science, 165,* 341-349, 1969.

Fornari, D. J. The geomorphic and structural development of Hawaiian submarine rift zones, *U.S. Geol. Surv. Prof. Pap., 1350,* 125 - 132, 1987.

Furumoto, A. S. and R. L. Kovach, The Kalapana earthquake of November 29, 1975: An intra-plate earthquake and its relation to geothermal processes, *Phys. Earth Planet. Inter., 18,* 197-208, 1979.

Hager, B. H. and R. W. Clayton, Constraints on the structure of mantle convection using seismic observations, flow models, and the geoid, in *Mantle Convection,* edited by W. R. Peltier, pp. 658-763, Gordon & Breach, New York, 1991.

Hill, D. P., Crustal structure of the island of Hawaii from seismic-refraction measurements, *Bull. Seismol. Soc. Am., 59,* 101-130, 1969.

Hill, D. P. and J. J. Zucca, Geophysical constraints on the structure of Kilauea and Mauna Loa volcanoes and some implications for seismomagmatic processes, *U.S. Geol. Surv. Prof. Pap., 1350,* 903-917, 1987.

Hoffmann, J. P., G. E. Ulrich and M. O. Garcia, Horizontal ground deformation patterns and magma storage during the Puu Oo eruption of Kilauea Volcano, Hawaii–Episodes 22-42, *Bull. Volcanol., 52,* 522-531, 1990.

Holcomb, R. T., Eruptive history and long-term behavior of Kilauea Volcano, *U. S. Geol. Surv. Prof. Pap. 1350, 1,* 261-350, 1987.

Jackson, D. B., D. A. Swanson, R. Y. Koyanagi and T. L. Wright, The August and October 1968 east rift eruptions of Kilauea Volcano, Hawaii, *U.S. Geol. Surv. Prof. Pap., 890,* 33 pp., 1975.

Kinoshita, W. K., H. L. Krivoy, D. R. Maby and R. R. MacDonald, Gravity survey of the Island of Hawaii, *U.S. Geol. Surv. Prof. Pap., 475-C,* C114-C116, 1963.

Klein, F. W., A linear gradient crustal model for south Hawaii, *Bull. Seismol. Soc. Am., 71,* 1503-1510, 1981.

Klein, F. W., User's guide to HYPOINVERSE, a program for computers to solve for earthquake locations and magnitudes, *U.S. Geol. Surv. Open File Rep., 89-314,* 1989

Klein, F. W., R. Y. Koyanagi, J. S. Nakata and W. R. Tanigawa, The seismicity of Kilauea's magma system, *U. S. Geol. Surv. Prof. Pap. 1350,* 1019-1186, 1987.

Koyanagi, R. Y., H. L. Krivoy and A. T. Okamura, The 1962 Kaoiki, Hawaii earthquake and its aftershocks, *Bull. Seismol. Soc. Am., 56,* 1317-1335, 1966.

Li, Y., C. H. Thurber, and C. G. Munson, profile of discontinuities beneath Hawaii from S to P converted seismic waves, *Geophys. Res. Lett., 19,* 111-114, 1992.

Lipman, P. W., The southwest rift zone of Mauna Loa: Implications for structural evolution of Hawaiian Volcanoes, *Am. J. Sci., 280-A,* 752-776, 1980.

Moore, J. G., and R. S. Fiske, Volcanic substructure inferred from dredge samples and ocean-bottom photographs, Hawaii, *Geol. Soc. Am. Bull. 80,* 1191-1202, 1969.

Rubin, A. M. and D. D. Pollard, Origins of blade-like dikes in volcanic rift zones, *U. S. Geol. Surv. Prof. Pap. 1350,* 1449-1470, 1987.

Ryan, M. P., The mechanics and three-dimensional internal structure of active magmatic systems: Kilauea Volcano, Hawaii, *J. Geophys. Res., 93,* 4213-4248, 1988.

Ryan, M. P., R. Y. Koyanagi and R. S. Fiske, Modeling the three-dimensional structure of macroscopic magma transport systems: Applications to Kilauea Volcano, Hawaii, *J. Geophys. Res., 86,* 7111-7129, 1981.

Swanson D. A., Magma supply rate at Kilauea Volcano, 1952 – 1971, *Science, 175,* 169–170, 1972.

Swanson, D. A., W. A. Duffield and R. S. Fiske, Displacement of the south flank of Kilauea Volcano: The result of forceful intrusion of magma into the rift zones, *U.S. Geol. Surv. Prof. Pap., 963,* 1-39, 1976.

Thurber, C. H., Seismic detection of the summit magma complex of Kilauea Volcano, Hawaii, *Science, 223,* 165-167, 1984.

Thurber, C. H., Seismic structure and tectonics of Kilauea Volcano, *U.S. Geol. Surv. Prof. Pap. 1350,* 919-934, 1987.

Thurber, C. H., and A. E. Gripp, Flexure and seisimicity beneath the south flank of Kilauea Volcano and tectonic implications, *J. Geophys. Res., 93,* 4271-4278, 1988.

Wilson, L., and J. W. Head III, Nature of local magma storage zones and geometry of conduit systems below basaltic eruption sites: Puu Oo, Kilauea East Rift, Hawaii, example, *J. Geophys. Res., 93,* 14,785-14,792, 1988.

Wright, T. L., Origin of Hawaiian tholeiite: a metasomatic model, *J. Geophys. Res., 89,* 3233 – 3252, 1984.

Yang, X., P. M. Davis, P. T. Delaney and A. T. Okamura, Geodetic analysis of dike intrusion and motion of the magma reservoir beneath the summit of Kilauea Volcano, Hawaii: 1970-1985, *J. Geophys. Res., 97,* 3305-3324, 1992.

R. W. Clayton and L. R. Rowan, Division of Geological and Planetary Sciences, Seismological Laboratory, 252-21 California Institute of Technology, Pasadena, CA 91125.

(Received November 30, 1990;
revised October 9, 1992;
accepted October 21, 1992.)